DC subsets and states unraveled across human juxtatumoral and malignant tissues

Kevin Mulder, Margaux Gardet, Wan Ting Kong, Amit Ashok Patel, Anne Calvez, Grégoire Gessain, Carlos de la Calle-Fabregat, Cécile Piot, Quentin Blampey, Elisa Poupaud, et al.

nature immunology

Article

https://doi.org/10.1038/s41590-025-02337-x

DC subsets and states unraveled across human juxtatumoral and malignant tissues

Received: 14 January 2023

Accepted: 9 October 2025

Published online: 8 December 2025

Check for updates

Kevin Mulder[1,19], Margaux Gardet[1,19], Wan Ting Kong[1], Amit Ashok Patel[1], Anne Calvez[2], Grégoire Gessain[1,3], Carlos de la Calle-Fabregat[1], Cécile Piot[4], Quentin Blampey[5,6], Elisa Poupaud[1], Ahmed-Amine Anzali[1], Garett Dunsmore[1], Antoine Bougouin[2], Guilhem Pupier[2], Lizhe He[7], Timothy Wiggins[7], Jiang He[7], George Emanuel[7], Anne-Gaëlle Goubet[1], Ghamdan Al-Eryani[8], Alexander Swarbrick[9,10], Judith Michels[11], Regine J. Dress[12], Marc Deloger[13], Antonio Bertoletti[14], Vincent Thomas de Montpreville[15], Catherine Sautès-Fridman[2], Wolf H. Fridman[2], Laurence Zitvogel[1], Florent Ginhoux[1,16,17,20] ✉ & Charles-Antoine Dutertre[1,18,20] ✉

Dendritic cells (DCs) are professional antigen-presenting cells. While plasmacytoid DCs (pDCs) are poor antigen-presenting cells at steady state, myeloid DCs (mDCs), which include DC1s, DC2s and DC3s, are specialized in T cell priming. To generate unbiased human DC atlases, we integrated DCs from 13 tumor tissues across 40 datasets to create a pDC + mDC-VERSE (DC-VERSE) and an mDC-VERSE single-cell RNA-sequencing compendium. We characterized DC subsets and 'states' across these tissues. Most studied tumors contained CD207$^+$ DCs, a subset of CD1c$^+$ DCs, whose expansion inversely correlated with tumor CD8$^+$ resident memory T cells, T cell clonality and the survival of patients treated with immune checkpoint inhibitors. Similarly to CCR7$^+$ mDCs (a common state of DC1s, DC2s and DC3s), we found that CD207$^+$ DCs were a common state of DC2s and DC3s. Spatially resolved single-cell transcriptomic and immunohistofluorescence analyses of human carcinomas demonstrated that lymphocytes and most DCs were enriched within the tumor stroma, while CD207$^+$ DCs were mostly embedded within tumor nests. These DC-VERSEs provide a robust resource available to the scientific community on DCs in health and pathology.

The mononuclear phagocyte (MNP) system initially encompassed monocytes and macrophages and later included conventional dendritic cells (cDCs)[1]. cDCs were defined as the sole potent activators of naive T cells and as 'accessory' cells bridging innate and adaptive immunity[2–4]. The discovery of common DC progenitors, including cDC1s (referred to here as DC1s), CD1c$^+$ DCs (initially termed cDC2s) and plasmacytoid DCs (pDCs), across tissues and species[5] clarified the cDC lineage and origin of major DC subsets[6–8]. High-dimensional single-cell technologies have unveiled additional subsets and states, particularly within human CD1c$^+$ DCs (DC2s and DC3s, collectively DC2s + DC3s) and pDCs[9–13]. CD123$^+$ DCs were shown to contain bona fide pDCs and pre-DCs[12,13], while CD1c$^+$ DCs contain CD5$^+$ DC2s and CD5$^-$CD14$^{+/-}$ DC3s, which expand during inflammation[9,11]. While DC1s and DC2s derive from common DC progenitors, DC3s may arise directly from granulocyte–monocyte progenitors and monocyte–DC progenitors[9,10]. It was established that 'cDCs' would qualify DCs derived from common DC progenitors and pre-DCs[5]. Thus, we classify DC1s, DC2s and DC3s as myeloid DCs (mDCs) due to their common myeloid progenitor origin.

A full list of affiliations appears at the end of the paper. ✉e-mail: Florent_Ginhoux@a-star.edu.sg; charles-antoine.dutertre@inserm.fr

https://doi.org/10.1038/s41590-025-02337-x

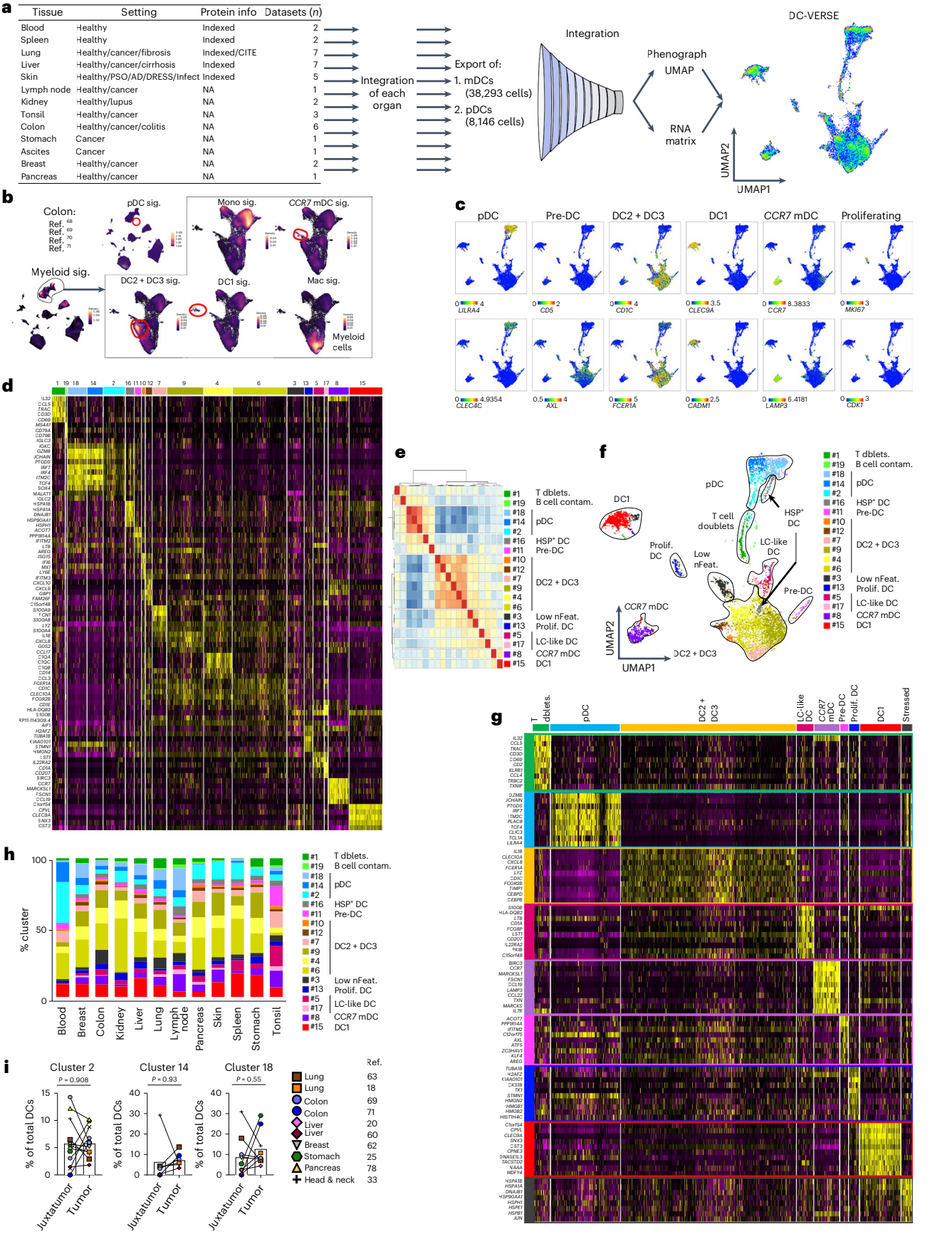

On the one hand, cell lineages and subsets are determined by their ontogeny; each subset corresponds to a differentiated cell population that arises from progenitor cells and is unable to cross-differentiate into another subset. To date, DC1s, DC2s and DC3s are the only three differentiated cell subsets among myeloid progenitor-derived DCs, and cells from one subset cannot convert to either of the others. On the other hand, cell states can be shared by different cell subsets and are molecular programs acquired during a cell's lifespan in

Fig. 1 | The DC-VERSE reveals signatures of major DC populations across human tissues. a, Summary of the integrated datasets and schematic overview of the meta-analysis. Integration was first performed at the organ level, and pDCs and mDCs were extracted. Extracted cells were then combined and integrated to generate the DC-VERSE. **b**, Strategy for delineating and extracting pDCs and mDCs (among total myeloid cells) from integrated colon datasets. Density plots showing the signatures used to define DC populations are displayed. See Supplementary Table 1 for the details of the studies. **c**, Signature genes of major populations (pDCs, pre-DCs, CD1c$^+$ DC2s + DC3s, DC1s, *CCR7* mDCs and proliferating DCs) are shown on the DC-VERSE UMAP space. **d**, Heatmap showing the expression of the top 5 DEGs per Phenograph cluster. **e**, Dendrogram clustering of Phenograph clusters. **f**, Overlay of the Phenograph clusters and corresponding megaclusters on the DC-VERSE UMAP. **g**, Heatmap showing the expression of the top 10 DEGs per megacluster. **h**, Composition of pDC and mDC clusters across juxtatumoral 'healthy' tissues. **i**, Percentage of pDC clusters in all integrated datasets between matched juxtatumoral and tumor tissues ($n = 10$). See Supplementary Table 1 for the details of the studies. Data are presented as mean values. *P* values were calculated using a Wilcoxon nonparametric paired test. PSO, psoriasis; AD, atopic dermatitis; DRESS, drug reaction with eosinophilia and systemic symptoms; Infect, infection; NA, not available; sig., signature; Mono, monocytes; Mac, macrophages.

response to specific tissue or inflammatory cues[14]. Thus, DC1s, DC2s and DC3s are mDC subsets, while C–C motif chemokine receptor 7 (CCR7)-expressing mDCs represent a mature state shared by DC1s, DC2s and potentially DC3s[15–20]. The expansion of single-cell RNA sequencing (scRNA-seq) has deepened, but also complicated, our understanding of DC heterogeneity. Inconsistent annotations of DC subsets across studies have created major confusion[14,19]. 'DC3' was first used for CD5$^-$CD14$^{+/-}$ 'CD1c$^+$ mDCs'[9–11] but later for populations transcriptionally aligned with CCR7$^+$ mDCs (mregDCs). Furthermore, CD207$^+$ DCs have been described in various contexts[21–24]. Consensus on how to define DC subsets versus states remains elusive, hindering comparisons across studies[14,19].

We previously unified monocyte and macrophage identities across 41 human scRNA-seq datasets[25]. Here, we apply a similar integrative framework to DCs and introduce the pDC + mDC-VERSE (DC-VERSE) and the mDC-VERSE, enabling in-depth analysis of DC heterogeneity and highlighting their potential roles in cancer. Notably, we identify a CD207$^+$CD1a$^+$ DC state that (1) accumulates inside the tumors of most cancers studied; (2) inversely correlates with T cell clonal expansion and CD8$^+$ resident memory T (T_{RM}) cells; (3) is predominantly embedded within tumor nests, while all the other DCs are mainly detected within the tumor stroma; (4) is associated with poor survival following immune checkpoint blockade (ICB), in contrast to DC1s and CCR7$^+$ mDCs; and (5) shows an impaired capacity to produce key cytokines. Altogether, these DC-VERSEs provide a comprehensive resource for dissecting DC heterogeneity across tissues and diseases, as well as a foundation for establishing a unified nomenclature for DC subsets and states (https://github.com/gustaveroussy/FG-Lab).

Results

DC-VERSE enables cross-study DC annotation

A previously published meta-analysis included human macrophages and monocytes sequenced from 41 published datasets across 13 tissues, including healthy, juxtatumoral and tumor tissues[25] (see 'Included studies' in Supplementary Table 1). The datasets were normalized and processed for their respective technologies as described in the Methods (Extended Data Fig. 1 and Supplementary Table 1). We used a comparable separate approach for DCs, integrating the datasets tissue by tissue. Then, the mDCs and pDCs were identified by their signatures, and the data were reintegrated to generate the DC-VERSE (Fig. 1a,b and Supplementary Table 1). To validate our integrated DC-VERSE, we used established gene transcripts, confirming the presence of pDCs (*LILRA4*/*CLEC4C*), pre-DCs (*CD5*/*AXL*), DC2s + DC3s (*CD1C*/*FCER1A*), DC1s (*CLEC9A*/*CADM1*), *CCR7* mDCs (*CCR7*/*LAMP3*) and proliferating DCs (*MKI67*/*CDK1*) (Fig. 1c). We used Phenograph[26] to define clusters and calculated the differentially expressed genes (DEGs) for all the clusters (cl. #) (Fig. 1d and Supplementary Table 1).

To balance biological context with conserved populations, we applied dendrogram clustering to examine the relationships between Phenograph clusters. This revealed ten major DC groups ('megaclusters') encompassing known populations and the distinct groups characterized here, including heat shock protein-expressing (HSP$^+$) DCs (cl. #16), low nFeature cells (Low nFeat., cl. #3), T cell doublets (T dblets., cl. #1) and Langerhans cell-like DCs (LC-like DC, cl. #5 and #17) (Fig. 1e,f). DEG analysis of megaclusters showed distinct signature genes for each (Fig. 1g and Supplementary Table 1), providing 'universal' signatures to identify DC populations in human scRNA-seq data. We next evaluated relative frequencies across juxtatumoral ('healthy') tissues (Fig. 1h). pDCs were highest in the blood, and we did not detect substantial differences in pDC frequencies between matched juxtatumoral and tumor tissues (Fig. 1i). Thus, the DC-VERSE unified human DC data, validated canonical types, defined ten signature megaclusters and found that pDCs are enriched in the blood, with no juxtatumor–tumor difference.

mDC-VERSE allows for granular annotation of myeloid-derived DCs

We aimed to enhance the resolution of mDCs, specifically focusing on DC2- and DC3-related cell subsets and states. The mDCs were extracted from integrated datasets tissue by tissue to generate the mDC-VERSE (Fig. 2a and Supplementary Table 1). Clusters were defined using Phenograph[26], and DEGs and differentially expressed regulons (DERs) were calculated for all Phenograph clusters (Extended Data Fig. 2a,b and Supplementary Table 1). Among these clusters, cl. #20 showed elevated expression of senescence-related genes, coupled with a relatively low nFeature_RNA (Low nFeat., Extended Data Fig. 2c); therefore, it was not functionally investigated further. Additionally, cl. #15, comprising only 118 cells (Minor, Extended Data Fig. 2d), was excluded from subsequent analyses due to its small sample size.

We examined the expression of well-established signature genes and proteins (cellular indexing of transcriptomes and epitopes by sequencing (CITE-seq) data by Maier et al.[18]) to broadly identify major DC subsets (Fig. 2a). Specifically, *TCF4*/*AXL* and CD45RA/CD123 protein expression characterized pre-DCs, while *CADM1*/*CLEC9A* and CD141/CD26 proteins identified DC1s (Fig. 2a). *FCER1A*/*CD1C* and CD33/CD1c proteins marked DC2s + DC3s; *CCR7*/*BIRC3*, along with programmed death ligand 1 (PD-L1) and PD-L2 proteins, denoted *CCR7* mDCs (Fig. 2a). Furthermore, *PCNA*/*MKI67* identified proliferating mDCs (prolif. mDC) (Fig. 2a). Notably, cl. #11 cells expressed T cell-specific membrane proteins, which likely represent T cell/DC doublets (Extended Data Fig. 2e). Dendrogram clustering was used to understand the relationships

Fig. 2 | The mDC-VERSE identifies mDC subsets and states across human tissues. a, Signature genes (from the mDC-VERSE; left) and protein markers (from the Maier CITE-seq data; right) of major DC subsets (pre-DCs, DC1s, DC subpopulations, *CCR7* mDCs and proliferating mDCs) are shown on the mDC-VERSE. **b**, Dendrogram clustering of Phenograph clusters to define megaclusters. **c**, Overlay on the mDC-VERSE of DC2 and DC3 cells defined based on CITE-seq CD5 and CD14 protein expression. **d**, Annotation of megaclusters within the UMAP space of the mDC-VERSE. **e**, Heatmap showing the relative expression levels of DERs between megaclusters common to the lung cancer (Maier)[18] and head and neck cancer (Cillo)[33] datasets. **f**, Ingenuity Pathway Analysis (IPA) of mDC megaclusters. Pathways were calculated using a right-tailed Fisher's exact test. **g**, Heatmap showing the scores of published DC signatures and nomenclature against DC megaclusters. Expr., expression; PRRs, pattern recognition receptors; NK cell, natural killer cell; Antigen pres., antigen presentation.

https://doi.org/10.1038/s41590-025-02337-x

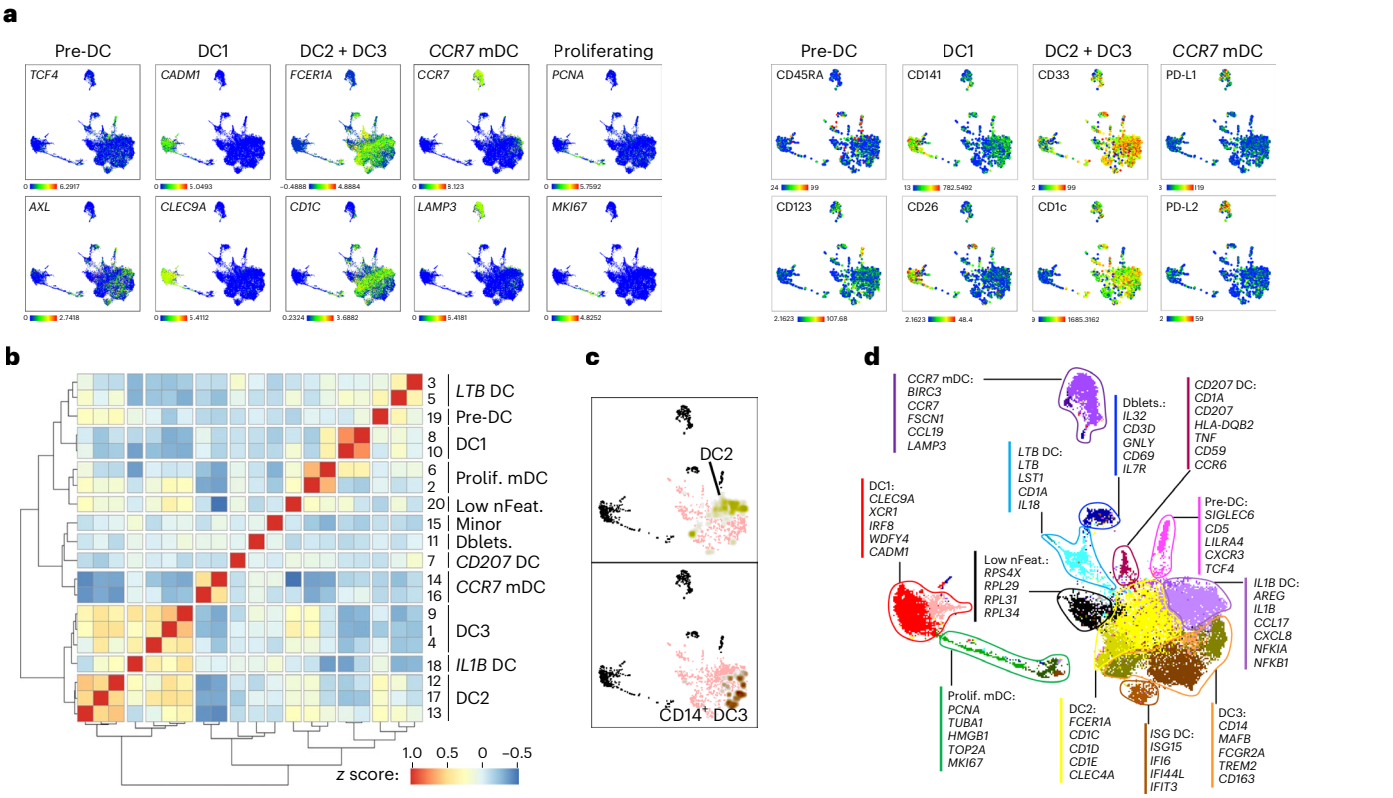

among Phenograph clusters, leading to the recognition of 12 mDC megaclusters (Fig. 2b and Supplementary Table 1). We identified regions encompassing previously defined subsets, including pre-DCs (cl. #19), DC1s (cl. #8 and #10), DC2s (cl. #12, #13 and #17), DC3s (cl. #1, #4 and #9), *CCR7* mDCs (cl. #14 and #16), proliferating mDCs (cl. #2 and #6) and T cell/DC doublets (cl. #11) (Fig. 2b). Furthermore, recent studies reported a distinct mDC subset, RORγt-expressing tolerogenic DCs[27,28]. Notably, the mDC-VERSE already distinguishes this population as cl. #3, whose DEGs largely overlap with those reported for RORγt-positive tolerogenic DCs[27] (Extended Data Fig. 2a and Supplementary Table 1).

Published CITE-seq data allowed us to quantify the expression of CD5 and CD14 proteins, thereby identifying CD5$^+$ DC2s and CD14$^+$ DC3s[18] (Fig. 2c and Extended Data Fig. 2g). Furthermore, published DC2 and DC3 gene signatures[11] confirmed the proper identification of DC2 and DC3 megaclusters (Extended Data Fig. 2h). The mDC-VERSE also delineated mDC populations that could not be clearly associated with the major mDC subsets described above, namely *CD207* DCs (cl. #7), *LTB* DCs (cl. #3 and #5) and *IL1B* DCs (cl. #18) (Fig. 2b). Lastly, although cl. #17 was clustered with DC2s, its unique interferon-stimulated gene (*ISG*) expression led to its classification as an independent megacluster termed *ISG* DCs (Fig. 2b,d and Extended Data Fig. 2a). Overall, the mDC-VERSE sharpened mDC resolution, validated canonical DC2/DC3 identities, resolved 12 megaclusters and uncovered additional populations (RORγt-like, *CD207*, *LTB*, *IL1B* and *ISG* DCs), while excluding artifactual and minor clusters.

mDC-VERSE standardizes granular mDC annotation

In addition to finding signature genes for widely recognized mDC subsets (pre-DCs, DC2s, DC3s and DC1s) and state (*CCR7* mDCs), the DEGs of megaclusters also identified genes for the less characterized or well-known DC states, such as *LTB* and *LST1* for *LTB* DCs; *CD1A*, *CD207* and *HLA-DQB2* for *CD207* DCs; *ISG15*, *IFI6*, *IFI44L* and *IFIT3* for *ISG* DCs; and *AREG*, *IL1B*, *CCL17* and *NFKB1* for *IL1B* DCs (Fig. 2d and Extended Data Fig. 2h,i). Because DC3s share transcriptomic and phenotypic similarities with monocytes[11], we aimed to address the potential contamination of monocyte-derived cells. We observed that the monocyte-derived DC (moDC) signature obtained from a published scRNA-seq study[29] mapped mostly within macrophages when overlapped onto the MNP-VERSE (Extended Data Fig. 2j)[25]. This signature could only be detected within the mDC-VERSE, with a lower mean expression within DC3 cl. #1 (Extended Data Fig. 2j,k). Moreover, several genes related to monocytes (*C1QA*, *C1QB*, *C1QC* and *CD14*) were also identified in the DEGs of DC3s (Extended Data Fig. 2a and Supplementary Table 1). When exploring only 'healthy' tissues (mostly juxtatumoral), DC populations were detected in varying frequencies, with some clusters such as *CCR7* mDCs, *LTB* DCs and *CD207* DCs detected in tissues but at a low frequency in the blood (Extended Data Fig. 2l,m). Of note, in the skin datasets, few Langerhans cells were detected and regrouped within the *CD207* DC cluster (Extended Data Fig. 2l,m).

DC2 + DC3 heterogeneity in humans has also been recognized[19], and two subsets of CD1c$^+$ DCs, namely CLEC4A$^+$ cDC2As (cDC2A_Brown) and cDC2Bs (cDC2B_Brown), have been described in the spleen[30], the latter being defined as expressing higher levels of *CLEC10A* (CD301) and *CLEC12A* (CD371)[30]. To define cDC2A, previous studies have regrouped cl. #3 and #4 described in their analysis[30]. Back-mapping these clusters (cl. #3 and #4, cDC2A_Brown) on the mDC-VERSE revealed that cl. #3 corresponded to *LTB* DCs, while cells from cl. #4 were detected within CD5$^+$ DC2s (Extended Data Fig. 2n). The heterogeneity of human DC2s + DC3s in various human tumors has been previously evaluated, describing six DC2 + DC3 subsets[31]. As these data were not integrated with the initial 40 datasets, we used multimodal reference mapping to project these populations onto the mDC-VERSE as a reference map[32]. We could observe to which megacluster these cells were assigned (Extended Data Fig. 3a,b). This method also showed that the mDC-VERSE could filter out cells with a low nFeature_RNA as they mapped to the mDC-VERSE cl. #20 (Extended Data Fig. 3c), allowing us to perform a second round of quality control to further identify and exclude low-quality cells for downstream analyses. When examining the mean expression of the top 50 DEGs of all DC2 + DC3 mDC-VERSE megaclusters on a previously published Uniform Manifold Approximation and Projection (UMAP)[31], we observed how the populations identified in this study corresponded to the mDC-VERSE megaclusters (Extended Data Fig. 3d,e) and vice versa (Extended Data Fig. 3f). The previously described cDC2_*ISG15* cluster corresponded to the *ISG* DCs, and the previously described cDC2_*FCN1* cluster corresponded to DC3s[31] (Extended Data Fig. 3b). In turn, cells with the signature of *LTB* DCs and *CD207* DCs (both defined within the mDC-VERSE) corresponded to unique subsets of the previously described cDC2_*CD1A* cells[31] (Extended Data Fig. 3e), highlighting the strength of the mDC-VERSE in identifying small discrete populations that might otherwise be missed.

After performing DEG analysis of the mDC-VERSE megaclusters, we used a gene regulatory network analysis (SCENIC: single-cell regulatory network inference and clustering) to identify megacluster-specific regulons common to two datasets from lung cancer[18] and head and neck cancer[33], which adequately represented the UMAP space (Fig. 2e and Supplementary Table 1). The regulons included *SOX4* and *KLF3* for pre-DCs; *IRF8*, *KLF8*, *FOXB1* and *HOXA7* for DC1s; *MEF2C* for DC2s; *MAFB*, *CEBPA* and *STAT2* for DC3s; *RXRA* and *RUNX3* for *CD207* DCs; *RFX2* for *LTB* DCs; and *ZEB1*, *IRF4* and *RELB* for *CCR7* mDCs (Fig. 2e). To gain insights into the biological processes and functional relevance of these cells, we performed pathway analysis on major DC megaclusters (Fig. 2f and Supplementary Table 1). We identified pathways including 'integrin signaling' and 'mTOR signaling' for *LTB* DCs, 'interleukin-10 (IL-10) signaling' and 'IL-6 signaling' for *IL1B* DCs, 'aryl hydrocarbon receptor (AHR) signaling' and 'DC maturation' for *CCR7* mDCs, 'phagosome formation' and 'complement system' for DC3s, and 'ERK/MAPK signaling' along with the hypoxia-related 'HIF1α signaling' pathway for *CD207* DCs (Fig. 2f).

Given the increased number of publications examining DC subsets and the lack of unity among these reports, various names have been assigned to DC subsets, creating confusion within the field[14]. The denomination 'DC3' was initially used to describe a subset of CD14$^+$ inflammatory DCs[11], while others have used DC3 to refer to DCs that have an apparent transcriptomic alignment to *CCR7* mDCs[18] due to the shared expression of transcripts such as *CCR7*, *BIRC3*, *FSCN1* and *LAMP3*, among others. Addressing the prevailing challenge of inconsistent nomenclature in the field of DC research[14], we sought to align the subsets identified in the mDC-VERSE with the published DEG signatures (Fig. 2g). This analysis aimed to unify the nomenclature of mDCs, which have been assigned multiple identities. It also demonstrated that the previously defined mature DC3s[34,35], mregDCs[18], *LAMP3* DCs[36,37] and *CCR7* DCs[38] all shared the gene expression signature of *CCR7* mDCs as defined here (Fig. 2g). While the previously defined DC3 signatures[11] could be appreciated (Fig. 2g), some previously published signatures displayed only weak alignment with DC2s or DC3s (Fig. 2g). Overall, the integrative approach used to generate the mDC-VERSE allowed us to appreciate the heterogeneity of mDCs and define the universal signatures of their subsets and states. Thus, we could reconcile the different studies that focused on the single-cell transcriptomic analysis of these cells.

Cancer shifts DC composition across matched tissues

To assess the importance of the identified DC subsets, a comprehensive metadata analysis was conducted comparing matched juxtatumoral tissues to tumors. Initially, DEG analyses were performed between matched juxtatumoral tissue and tumor across all mDCs (Fig. 3a,b and Supplementary Table 1). Notable DEGs, including *SPP1*, *CD14*, *LTB*, *CD1A*, *BIRC3* and *CD207*, were found to be upregulated in tumors, whereas *CLEC9A* (a DC1-specific gene) and *CPVL* were found to be enriched in

the juxtatumoral tissues (Fig. 3a). Several of the DEGs corresponded to the mDC-VERSE megacluster DEGs (Fig. 2a and Supplementary Table 1), prompting an exploration of their relative proportions across matched tissues. A global comparison of megacluster proportions indicated a potential increase in *CCR7* mDCs, *ISG* DCs, *CD207* DCs and *LTB* DCs in tumors (Fig. 3c and Extended Data Fig. 4a). For datasets where tumor localization was available (that is, juxtatumoral tissue, tumor periphery and tumor core had been analyzed separately), we observed that *CCR7* mDCs tended to accumulate in the tumor periphery, while proliferating mDCs tended to accumulate in the tumor core (Extended Data Fig. 4b). Additionally, the ratio of DC3s to DC2s (DC3/DC2 ratio), representing functionally similar but proinflammatory counterparts, showed an increasing trend in the tumor core (Extended Data Fig. 4a,b). A meta-analysis was then conducted on studies with matched juxtatumoral and tumor samples across the identified mDC-VERSE megaclusters, incorporating previously predicted clusters[31] (Fig. 3d and Extended Data Fig. 4c,d). Thus, this meta-analysis revealed a significant increase of *CD207* DCs in tumors, while the DC3/DC2 ratio and the frequencies of *ISG* DCs, *CCR7* mDCs and proliferating mDCs significantly accumulated in most, but not all, tumors (Fig. 3d,e). A significant decrease in DC1s was also observed in tumors (Fig. 3d,e). When examining the composition of proliferating mDCs using label transfer (Seurat v4), the frequency of *CD207* DCs among proliferating mDCs exhibited a 10.75-fold increase in the tumor relative to juxtatumoral tissue (Fig. 3f). Moreover, compared to other megaclusters, *CD207* DCs and DC1s exhibited a greater percentage of proliferation in the tumor than in their matched juxtatumoral tissue (Fig. 3g). Overall, our metadata analysis underscores a key shift in DC populations within the tumor microenvironment, particularly the expansion of *CD207* DCs, *CCR7* mDCs, *ISG* DCs and proliferating mDCs, alongside a notable decrease in DC1s, with *CD207* DCs exhibiting a marked increase within the proliferating mDC population.

NSCLC tumors remodel DC subsets across matched tissues

Next, we conducted a validation study using multiparametric flow cytometry in matched juxtatumoral tissues and tumors from eight patients with non-small-cell lung carcinoma (NSCLC) (Fig. 4 and Supplementary Table 1). Among CD45$^+$ leukocytes, MNPs were initially identified, from which we distinguished CD123$^+$ pre-DCs + pDCs, DC1s, DC2s + DC3s, and monocytes and macrophages (Fig. 4a and Extended Data Fig. 5a). MNPs were exported and reanalyzed, revealing all major MNP subsets (Fig. 4b and Extended Data Fig. 5b,c). The frequencies of DC1s, total CD1c$^+$ DC2s + DC3s, pDCs and pre-DCs were comparable between juxtatumoral and tumor tissues (Fig. 4c). Next, we focused on specific DC populations, including DC2s and DC3s, where an increased percentage of CD14$^+$ DC3s was observed in the tumors of six of the eight patients (Fig. 4d,e).

When examining the total DC3 population (including CD14$^-$ DC3s), we observed a trend toward an increased DC3/DC2 ratio in tumor samples for seven of the eight patients, supporting the metadata findings of the mDC-VERSE (Fig. 4f). CITE-seq data further demonstrated that the CD103 protein was expressed on the membrane of all *LTB* DCs and some *CD207* DCs (Extended Data Fig. 5d). However, CD103$^+$ *LTB* DCs were not expanded in lung tumors (Fig. 4g,h). The mDC-VERSE revealed that the *CD207* and *CD1A* genes were highly expressed by *CD207* DCs defined in the mDC-VERSE. We confirmed that the frequency of CD1a$^+$CD207$^+$ DCs was similarly increased in the tumor tissue of all patients with lung cancer, with a fold increase ranging from 1.48 to 209.11 (Fig. 4i,j and Extended Data Fig. 5e). Thus, across matched NSCLC tissues, the DC composition was broadly conserved, but tumors consistently showed higher frequencies of DC3s and CD1a$^+$CD207$^+$ DCs.

mDC-VERSE distinguishes mDC subsets from states

The term 'lineage' is conventionally used to describe a population of cells that arises from dedicated progenitors with known transcription factors regulating their differentiation across tissues[5,14,38,39], while 'state' is usually used to refer to a transient or inducible configuration—activation, maturation, stress, metabolic status or cell cycle status—at a particular moment in time and can be imprinted across distinct lineages[38]. Using computational techniques, including label transfer and Connectivity Map (CMap) analysis[40,41], our study investigated mDC populations (*CD207*, *IL1B*, *LTB* and *ISG* DCs) and deciphered their categorization as either cell subsets or states (Fig. 5a,b and Extended Data Fig. 6a). Both approaches indicated that *CCR7* mDCs represented a common maturation state shared by DC1s, DC2s and DC3s (Fig. 5a,b and Extended Data Fig. 6a). Meanwhile, the *CD207*, *LTB*, *ISG* and *IL1B* mDC megaclusters appeared to be in a transcriptomic state shared by DC2s and DC3s (Fig. 5a,b and Extended Data Fig. 6a). For simplicity and clarity, we will refer to these populations as DCs while acknowledging their shared cell type.

Within the spectral flow cytometry data in NSCLC, we analyzed CD1a, CD207 and CD103 at the protein level to determine whether cells expressing these membrane proteins correspond to unique subsets of CD1c$^+$ DCs or whether they correspond to cell 'states' that could be acquired by DC2s and/or DC3s (Fig. 5c and Extended Data Fig. 6b). Alongside this, we also investigated the CCR7 state to confirm the transcriptomic observations. These analyses revealed that the *CCR7* mDC state, defined here as HLA-DR^{hi}CCR7^{hi} cells (CCR7$^+$ mDCs), is a shared maturation state of DC1s (CCR7$^+$ DC1s), DC2s (CCR7$^+$ DC2s) and DC3s (CCR7$^+$ DC3s) (Fig. 5c and Extended Data Fig. 6b). Likewise, CD103$^+$ *LTB* DCs and CD207$^+$ DCs corresponded to shared phenotypic states of CD5$^+$ DC2s and CD5$^-$CD14$^{+/-}$ DC3s (CD103$^+$ or CD207$^+$ DCs, respectively), as they did not constitute a specific subset of either DC2s or DC3s (Fig. 5c and Extended Data Fig. 6b). Note that a minor fraction of DC1s was detected within CD103$^+$ cells (Extended Data Fig. 6b,c). Beyond CD5 and CD14, these CD103$^+$ and CD207$^+$ cell states also showed variable expression of other markers commonly expressed by DC3s, such as CD38 and CD11b (Extended Data Fig. 6d). Upon comparing juxtatumoral and tumor tissues, a significantly increased frequency of CCR7$^+$ DC1s was observed in tumors (Fig. 5d,e). In contrast, the frequencies of total CCR7$^+$ DCs (as well as CCR7$^+$ DC2s or CCR7$^+$ DC3s) were not significantly different (Fig. 5d,e and Extended Data Fig. 6g).

To further understand the state program of *CD207* DCs, we examined bulk RNA-seq data from cultured DC2s and DC3s[42]. DC2s and DC3s were cultured with or without transforming growth factor-β (TGFβ), which can induce CD207 expression[43]. When performing gene set enrichment analysis (GSEA) with the DEGs of *CD207* DCs obtained from the mDC-VERSE analysis, we observed a significant upregulation

Fig. 3 | Metadata analysis of mDC populations in cancer. a,**b**, Volcano plot (**a**) and meaning plots (**b**) of DEGs between globally matched juxtatumoral tissue and tumor for all cells included in the mDC-VERSE. **c**, Bar plot showing the percentage of megaclusters (left), with density plots of globally matched juxtatumoral tissue and tumor (right). **d**, Percentage of each mDC megacluster of the mDC-VERSE in all integrated datasets and query datasets (mapped through multimodal reference mapping and annotated with cross symbols) between matched juxtatumoral tissue and tumor. Only datasets with a minimum of eight detected cells were plotted; datasets were plotted for *CCR7* mDCs ($n = 14$), DC1s ($n = 16$), DC2s ($n = 16$), DC3s ($n = 15$), proliferating mDCs ($n = 13$), *CD207* DCs ($n = 8$), *ISG* DCs ($n = 13$) and the DC3/DC2 ratio ($n = 14$). Box plots are presented as mean values. **e**, Overview of all included cancer datasets depicting a change in the distribution of DC populations between juxtatumoral tissue and tumor. **f**, Percentage of DC megaclusters predicted through label transfer (Seurat v4) within the proliferating mDC megacluster, with the corresponding fold change (tumor versus juxtatumoral tissue). **g**, Percentage of proliferating cells within each DC megacluster in juxtatumoral and tumor tissues. See Supplementary Table 1 for the specified studies and tumor types. All *P* values were calculated using a two-tailed Wilcoxon test. MM, multiple myeloma.

https://doi.org/10.1038/s41590-025-02337-x

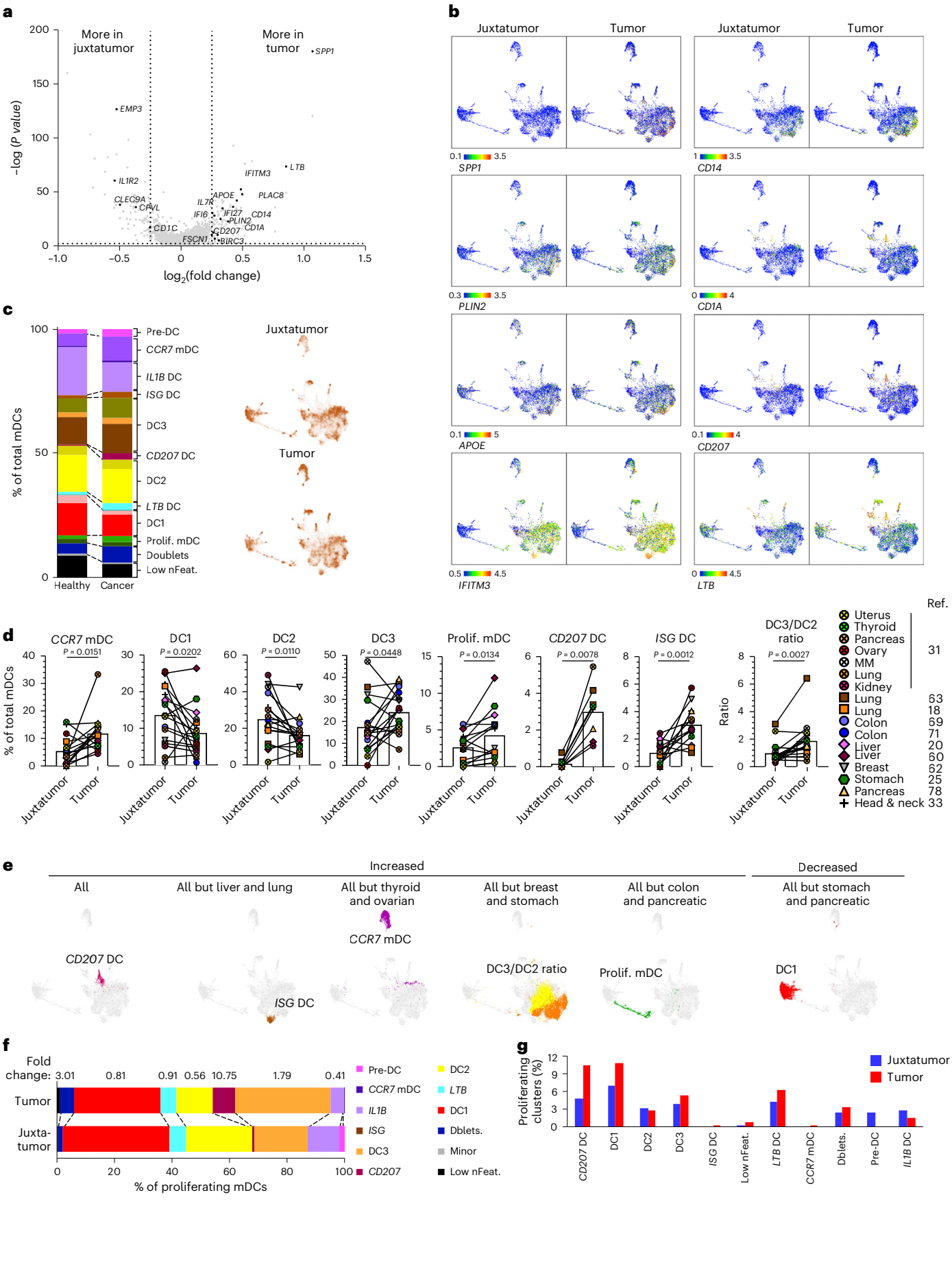

https://doi.org/10.1038/s41590-025-02337-x

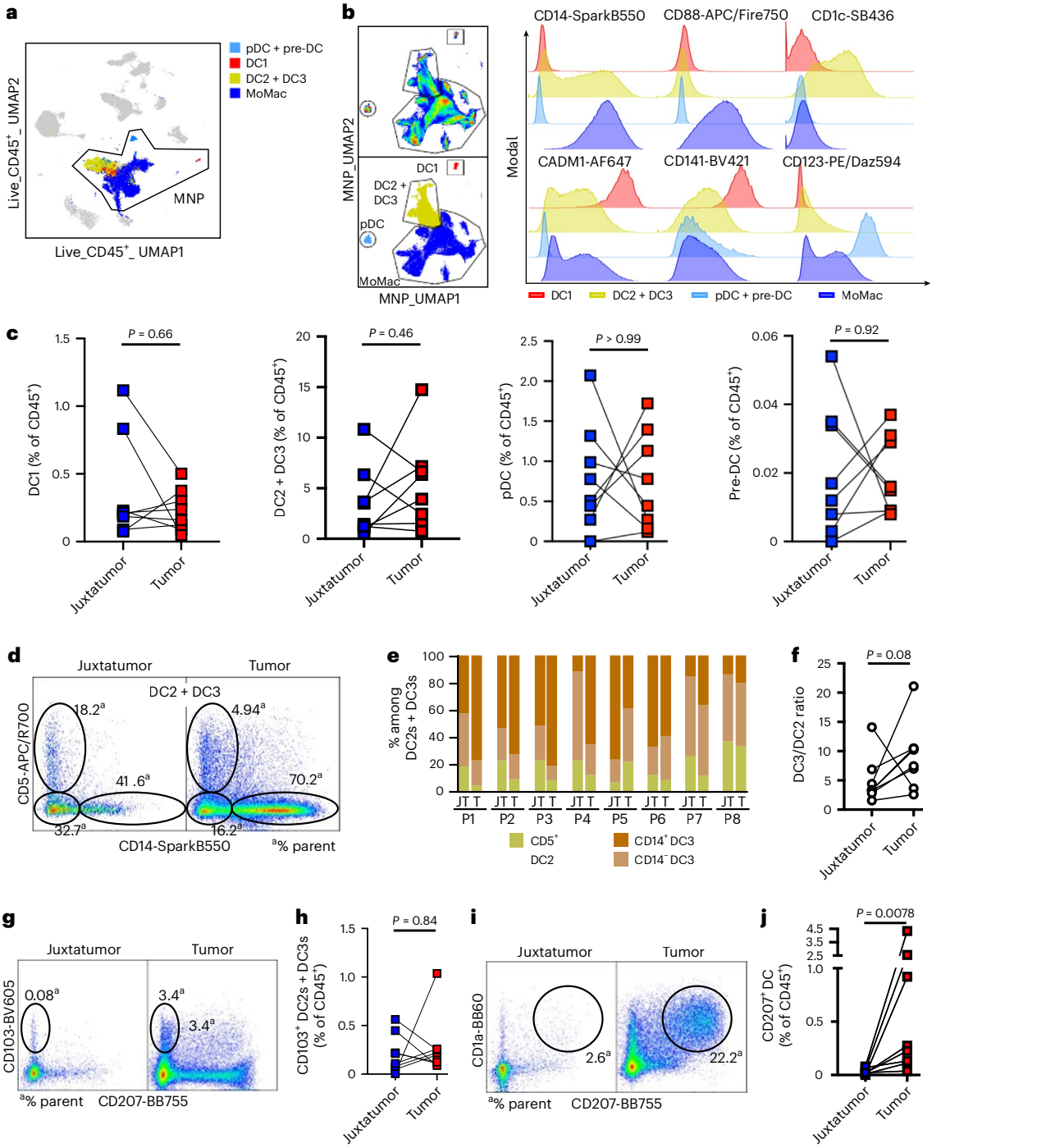

Fig. 4 | Spectral flow cytometric analysis of DC subsets and states in eight patients with NSCLC. a, UMAP of singlet, live, CD45$^+$ cells from juxtatumoral and tumor samples obtained from eight patients with NSCLC. **b**, UMAP of extracted MNPs showing delineation of DC1s, DCs, CD123$^+$ DCs (pDCs and pre-DCs; Extended Data Fig. 5c) and monocytes/macrophages. Histograms show the expression of selected markers by cells defined in the UMAP of extracted MNPs (right panels). **c**, Percentage of DC1s, CD1c$^+$ DC2s + DC3s, pDCs and pre-DCs among the total CD45$^+$ cells ($n = 8$). **d**–**f**, Identification (**d**) and quantification (**e**) of DC2s and DC3s, along with the DC3/DC2 ratio (**f**), in juxtatumoral and tumor samples ($n = 8$). **g**,**h**, Identification (**g**) and percentage (**h**) of CD103$^+$ *LTB* DCs among the total CD45$^+$ cells ($n = 8$). **i**,**j**, Identification (**i**) and percentage (**j**) of CD207$^+$ DCs among the total CD45$^+$ cells ($n = 8$). All *P* values were calculated using a two-tailed Wilcoxon test. MoMac, monocytes/macrophages; JT, juxtatumor; T, tumor.

of this signature in day 3 cultured cells from both the DC2 and DC3 sorted populations under TGFβ stimulation (Fig. 5f). Notably, in the DC3 population cultured as described above but also stimulated with the Notch ligand (coculture with OP9-DL4), this upregulation was significantly higher compared to that in DC3s stimulated with TGFβ alone (Extended Data Fig. 6h), indicating that both DC2s and DC3s can acquire a *CD207* state and that the Notch ligand further enhances this phenotype. Of note, the *RUNX3* and *RXRA* regulons, which are activated downstream of TGFβ receptor signaling, were specific to *CD207* DCs defined in the mDC-VERSE (Fig. 2e), strengthening the hypothesis that TGFβ could drive the acquisition of the *CD207* DC state in vivo.

Next, to confirm the transcriptional program in CD207$^+$ cells, we sorted primary CD207-negative and CD207-positive CD1c$^+$ DCs from ovarian cancer samples and performed bulk RNA-seq

https://doi.org/10.1038/s41590-025-02337-x

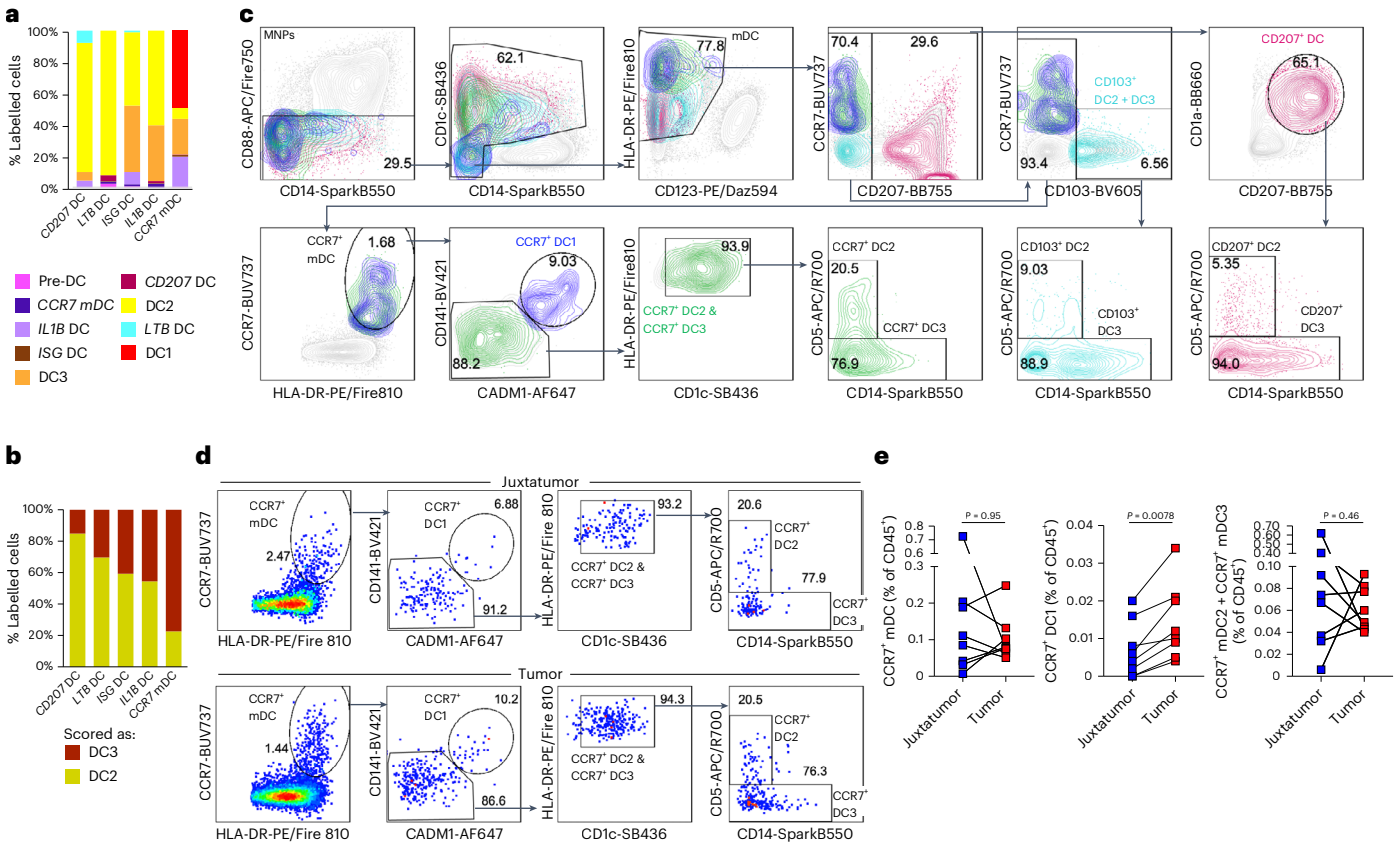

Fig. 5 | Consideration of subsets versus states. a, Percentage of DC megaclusters predicted through label transfer (Seurat v4) within the proliferating mDC megacluster, with the corresponding fold change (tumor versus juxtatumoral tissue). **b**, CMap analysis of identified cell states showing their enrichment for DC2 or DC3 gene sets. The CMap permutation *P* value was <0.05. **c**, Gating strategy of the different states of DCs starting from total MNPs extracted from all concatenated data obtained for tumor samples. The percentage of each gate is displayed. **d**,**e**, Identification (**d**) and percentage (**e**) of total CCR7$^+$ mDCs, CCR7$^+$ DC1s and CCR7$^+$ DC2s + DC3s among the total CD45$^+$ cells ($n = 8$). **f**, GSEA of the *CD207* DC signature comparing bulk RNA-seq of DC2s and DC3s on days 0 and 3 of a culture treated with GM-CSF + TGFβ from Kvedaraite et al.[42]. **g**, GSEA of the *CD207* DC signature of FACS-sorted CD207$^+$ and CD207$^-$ CD1c$^+$ DCs from ovarian cancer samples. **h**, Mean signature of the top 25 genes from FACS-sorted CD207$^+$ and CD207$^-$ CD1c$^+$ DCs from ovarian cancer samples on the mDC-VERSE. NES, normalized enrichment score.

(Extended Data Fig. 6i). The *CD207* DC signature obtained from the mDC-VERSE was significantly upregulated in CD207$^+$ DCs compared to CD207$^-$ DCs (Fig. 5g). Conversely, plotting the top 25 significant DEGs of fluorescence-activated cell sorting (FACS)-sorted CD207$^+$ DCs showed specific expression in the *CD207* DC population of the mDC-VERSE (Fig. 5h and Supplementary Table 1), supporting the notion that the 'CD207' state was similar in the protein and RNA annotation. Therefore, integrated multiomic analyses revealed key mDC phenotypes as shared, inducible states across DC subsets.

Tumors compartmentalize DC subsets and states

We next explored the spatial distribution of DC subsets defined in the mDC-VERSE within tumor lesions from three patients with triple-negative breast cancer and two patients with estrogen receptor-positive breast cancer[44] (Fig. 6a,b and Extended Data Fig. 7a,b). We reanalyzed Visium spatial data of breast cancer tumors[44], where we performed *z*-scoring of mDC transcriptomic signatures identified in the mDC-VERSE. Most DC subsets and states were found in immune-enriched and tertiary lymphoid structure niches, including *CD207* DCs (Fig. 6b). *CD207* DCs, and to a lesser extent *IL1B* DCs, were also detected in the 'invasive cancer + stroma' niche (Fig. 6b). To better define the in situ localization of DC subsets and states at single-cell resolution, breast and lung tumors were analyzed using MERSCOPE (Vizgen). After the delineation of cells within tissue cross-sections (segmentation), we conducted a principal component (PC) analysis (PCA) followed by UMAP projection using PCs selected for their high loading with immune-related genes (Extended Data Fig. 7c and Supplementary Table 1). This identified major cell populations, including *EPCAM*-expressing tumor cells,

https://doi.org/10.1038/s41590-025-02337-x

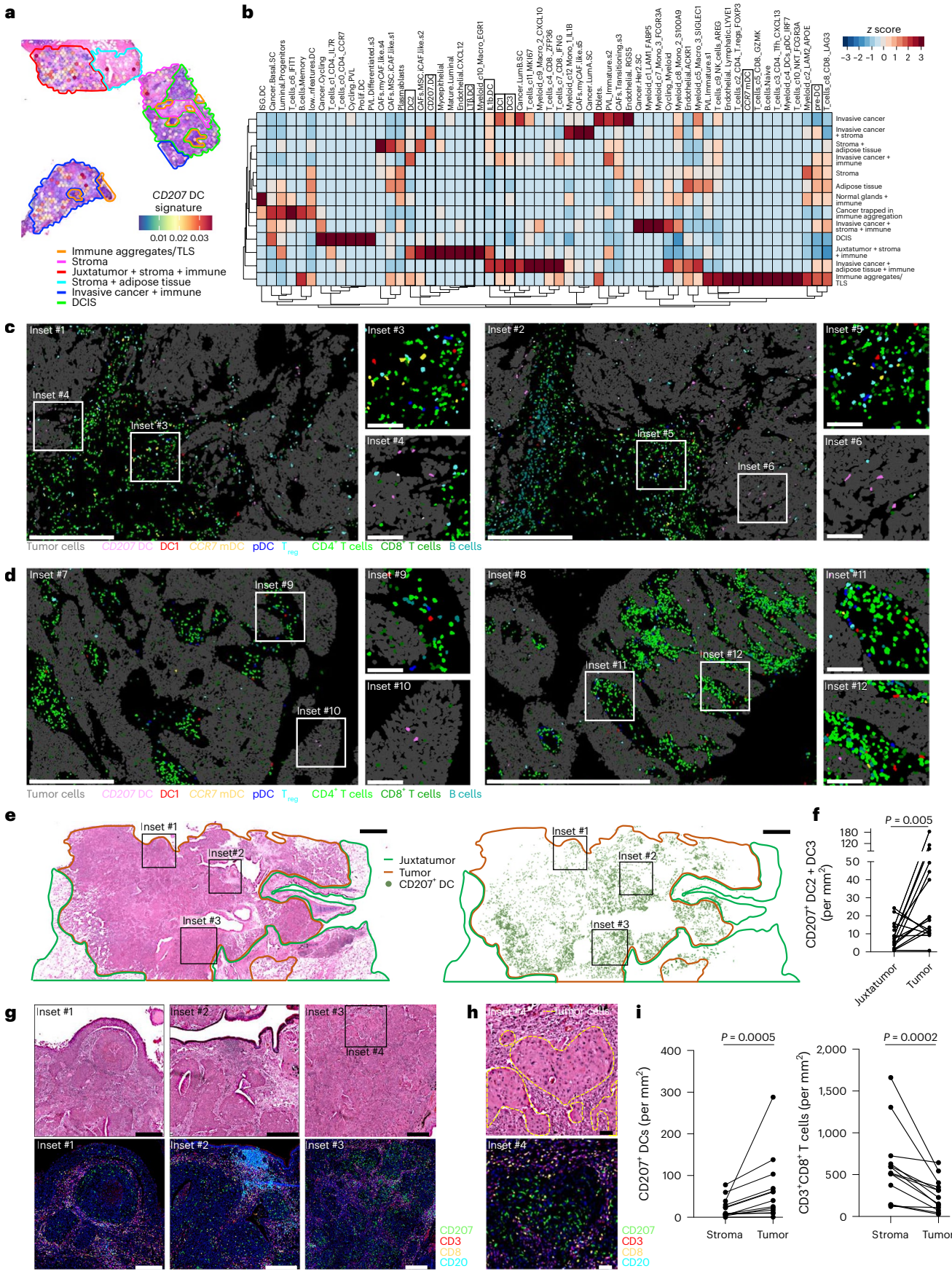

Fig. 6 | Spatial analysis of DC subsets and states in lung and breast tumors. **a**, Visium spatial transcriptomic profiling of triple-negative breast cancer tumors (initially published by Wu et al.[44]), outlining various tissue compartments in addition to spots showing the scaled median enrichment of the *CD207* DC signature, overlaid on hematoxylin and eosin (H&E)-stained images. **b**, Heatmap depicting the correlation of both immune and nonimmune cell types within tissue niches. Certain nonimmune populations were mapped using the nomenclature and signatures from the study of Wu et al. **c**,**d**, Visualization of the insets defined in Extended Data Fig. 7f. Tumor cells and immune cells (scale bar of insets #1, #2, #7 and #8, 500 µm; scale bar of insets #3–#6 and #9–#12, 100 µm) in breast (**c**) and lung (**d**) tumor cross-sections were visualized using MERSCOPE (Vizgen). **e**, Visualization of a full NSCLC formalin-fixed paraffin-embedded (FFPE) cross-section where juxtatumoral tissues and tumor regions are delineated by green and brown lines, respectively, and where insets #1 to #3 (magnified in **g**) are depicted (scale bar, 0.2 cm). The Halo software allowed us to perform an unsupervised delineation of the stroma and tumor area in only 13 of the 16 stained cross-sections. The H&E-stained image (scale bar, 0.2 cm; left) and the spatial mapping of $CD207^+$ cells ($CD207^+$ DCs; right) of the same tumor cross-section are shown. **f**, Density of $CD207^+$ DCs in juxtatumoral tissue and tumor regions from the 16 NSCLC tumors analyzed. **g**, Magnification of the insets (scale bar, 0.5 mm) defined in **e**. **h**, H&E-stained image (top) and the multiplexed fluorescent image (bottom) from inset #4 (defined in **g**) (scale bar, 0.1 mm). The yellow dotted line delineates the tumor glandular areas from the tumor stroma. **i**, Density of $CD207^+$ DCs (left) and $CD3^+CD8^+$ T cells (right) from 13 of the 16 NSCLC tumors that could be analyzed for tumor versus stroma regions. *P* values in **f** and **i** were calculated using the two-tailed Wilcoxon paired nonparametric test. TLS, tertiary lymphoid structure; DCIS, ductal carcinoma in situ.

fibroblasts, endothelial cells and *PTPRC* (CD45)-expressing immune cells (Extended Data Fig. 7c). Immune cells were next extracted and analyzed as described above, revealing some B cells, subsets of T cells ($CD4^+$ T cells, CD4- and FOXP3-expressing regulatory T (T_{reg}) cells, and $CD8^+$ T cells), monocytes, macrophages and DC populations, including *CLEC4C* (CD303)- and *IL3RA* (CD123)-expressing pDCs (Extended Data Fig. 7d). Notably, *CD207* DCs expressed the highest quantity of tumor necrosis factor (*TNF*) transcripts among all immune cells (Extended Data Fig. 7d), consistent with our observation from the mDC-VERSE where *TNF* was a top DEG of *CD207* DCs (Fig. 2d). We next extracted and reanalyzed mDCs, allowing us to identify *CCR7* mDCs, DC1s, $CD207^-$ DCs and $CD207^+$ DCs (Extended Data Fig. 7c–e). The above-mentioned cell populations were then mapped onto the lung and breast tumor cross-sections (Extended Data Fig. 7f), in which insets were defined to better visualize the localization of each immune cell population (Fig. 6c,d). pDCs, *CCR7* mDCs and DC1s were detected within the tumor stroma in close contact with B cells and T cells, while *CD207* DCs were located within tumor nests in both cancers (Fig. 6c,d). In addition to the *CD207* DCs, a few T_{reg} cells and $CD8^+$ T cells were detected within tumor nests in both cancers (Fig. 6c,d).

To validate the tumor nest localization of $CD207^+$ DCs in a larger number of patients, immunohistofluorescence (IHF) analyses were conducted on NSCLC tumors obtained from 16 patients, where the CD207, CD3, CD8 and CD20 proteins were stained simultaneously (Fig. 6e–i and Extended Data Fig. 7g). By reanalyzing our spectral flow cytometry data in NSCLC, we confirmed that, among the live cells of the NSCLC tumor, CD207 expression was observed only within $CD45^+CD1a^+CD1c^+HLA\text{-}DR^+HLA\text{-}DP^+$ cells (all markers of $CD207^+CD1a^+$ DCs; Extended Data Fig. 6e). Thus, staining for the CD207 membrane protein is sufficient to identify $CD207^+$ DCs specifically. Juxtatumoral and tumor regions were defined by a pathologist and are delineated in green and brown, respectively (Fig. 6e). Automated quantifications confirmed the significantly higher density of $CD207^+$ DCs in the tumor compared to the juxtatumoral lung tissue (Fig. 6e,f). Tertiary lymphoid structures were detected (inset #2), and $CD207^+$ DCs were excluded from these structures (Fig. 6g and Extended Data Fig. 7g). Within the tumor, $CD3^+$ T cells (including $CD3^+CD8^+$ T cells) and $CD20^+$ B cells predominantly accumulated in the tumor stroma, while $CD207^+$ DCs were primarily detected in tumor nests, particularly in glandular structures (Fig. 6g,h and Extended Data Fig. 7g). Quantitative analyses confirmed the significantly higher density of $CD207^+$ DCs in the tumor nests compared to the tumor stroma, while the opposite was quantified for $CD3^+CD8^+$ T cells (Fig. 6h,i). Thus, these data confirmed the intratumoral accumulation of $CD207^+$ DCs and showed that they were embedded between tumor cells, while the other DC populations, as well as T and B cells, were mostly detected within the tumor stroma.

CD207 DCs are associated with an unfavorable outcome in cancer

To gain more insight into the functional properties of DCs with a specific focus on $CD207^+$ DCs, we isolated primary lung tumor cells, digested them and cultured them overnight. Intracellular cytokine staining revealed that $CD1c^+CD207^+$ DCs spontaneously produced significantly lower levels of the cytokines TGFβ and TNF, with a similar trend observed for IL-6 and IL-10, compared to $CD1c^+CD207^-$ DCs (DC2s + DC3s) (Fig. 7a and Extended Data Fig. 8a). No observable change in costimulatory markers (CD40, CD80 and CD86) was noted (Extended Data Fig. 8b). When examining the state of $CCR7^+$ mDCs in DC1s and $CD1c^+$ DCs (DC2s + DC3s), we observed a significant increase in the levels of multiple cytokines, including IL-12, IL-10 and TNF, specifically in the $CCR7^+$ DC1 subset, as compared to their $CCR7^-$ counterparts (Fig. 7b). CCR7-expressing $CD1c^+$ DCs showed a significant increase only in IL-10 production (Fig. 7c). Regarding the costimulatory markers, we observed increased expression of CD80 and CD86 only in $CCR7^+$ DC1s compared to $CCR7^-$ DC1s, while only a trend toward increased expression was noted in $CCR7^+$ $CD1c^+$ DCs compared to $CCR7^-$ $CD1c^+$ DCs (Extended Data Fig. 8b).

Because mDCs are professional antigen-presenting cells that can prime naive T cells or reactivate memory T cells, we explored the potential relationship between mDCs and T cells. To address this, we mapped a public breast cancer dataset[45] onto the mDC-VERSE using

Fig. 7 | Characterization of the pathophysiological involvement of mDC populations in human patients with cancer. **a**–**c**, Percentage of positive cells for cytokine production from cells gated as $CD1c^+$ DC2s + DC3s split on $CD207^{+/-}$ ($n = 5$ patients) (**a**), $CADM1^+$ DC1s split on $CCR7^{+/-}$ ($n = 6$ patients) (**b**) and $CD1c^+$ DC2s + DC3s split on $CCR7^{+/-}$ ($n = 6$ patients) (**c**). Data are presented as mean values ± s.e.m. **d**, Percentage of predicted megaclusters by multimodal reference mapping of query data from patients with breast cancer categorized by T cell clonality and treatment status (ICB = anti-PD-1 therapeutic monoclonal antibody). **e**, DC1/*CD207* DC ratio for patients from the study of Bassez et al.[45], with at least one in either population. **f**, Pearson correlation between the percentage among *PTPRC* (CD45)-expressing immune cells of *CD207* DCs ($n = 8$), *CCR7* mDCs ($n = 7$), *ISG* DCs ($n = 6$) or DC1s ($n = 8$) against the total *CD8* T cells (top), *CD8* T_{RM} cells (middle) or *CD8* T_{EMRA} cells (bottom). **g**, Correlation between the frequencies of *CD207* DCs and *CD8* T_{RM} cells among immune cells in lung tumors within the scRNA-seq data from Leader et al.[23] ($n = 28$). The cutoff was determined by the local density minimum (antimode) identified on the kernel density estimation curve. **h**, Pearson correlation between the frequencies (among $CD45^+$ cells) of *CD207* DCs, DC1s, $CCR7^+$ DC1s, $CCR7^+$ DC2s and $CCR7^+$ DC3s against $CD8^+$ T cells. Data were from a flow cytometry analysis of tumor cells obtained from eight patients with NSCLC ($n = 8$). **i**, Kaplan–Meier plot of the overall survival of patients with different cancers whose tumors were sampled and analyzed by bulk RNA-seq before ICB treatment. Patients were separated based on the high or low expression of the mDC populations' mean gene signatures (left and middle panels) or the ratio of *XCR1* to *CD207* transcripts (right panel). *P* values were calculated using a two-tailed Wilcoxon nonparametric paired test. Correlations were evaluated using the Pearson correlation coefficient (*r*) with a two-tailed test. *$P < 0.05$. HR, hazard ratio.

https://doi.org/10.1038/s41590-025-02337-x

multimodal reference mapping[32], where T cell clonality was evaluated before and after chemotherapy with or without anti-programmed cell death protein 1 (anti-PD-1) therapy (Fig. 7d–f, Extended Data Fig. 9a and Supplementary Table 1). In contrast to *CCR7* mDCs, *ISG* DCs and DC1s, the proportion of *CD207* DCs among the total DCs tended to increase only in tumors from patients without clonal T cell expansion when treatments were analyzed separately (Fig. 7d and Extended Data Fig. 9b). However, when the treatment groups were combined, the overall percentage of *CD207* DCs was significantly increased in patients without clonal T cell expansion (Extended Data Fig. 9c). Notably, T cell clonal expansion was observed only in patients with a DC1/*CD207* DC ratio of >1 (both before and after treatment) (Fig. 7e). If validated in other cohorts, the DC1/*CD207* DC ratio could become a means of predicting T cell clonality within tumors. Further analysis using published annotations of T cells correlated mDC-VERSE populations with effector memory T cells that reexpress CD45RA (T_{EMRA} cells), T_{RM} cells and

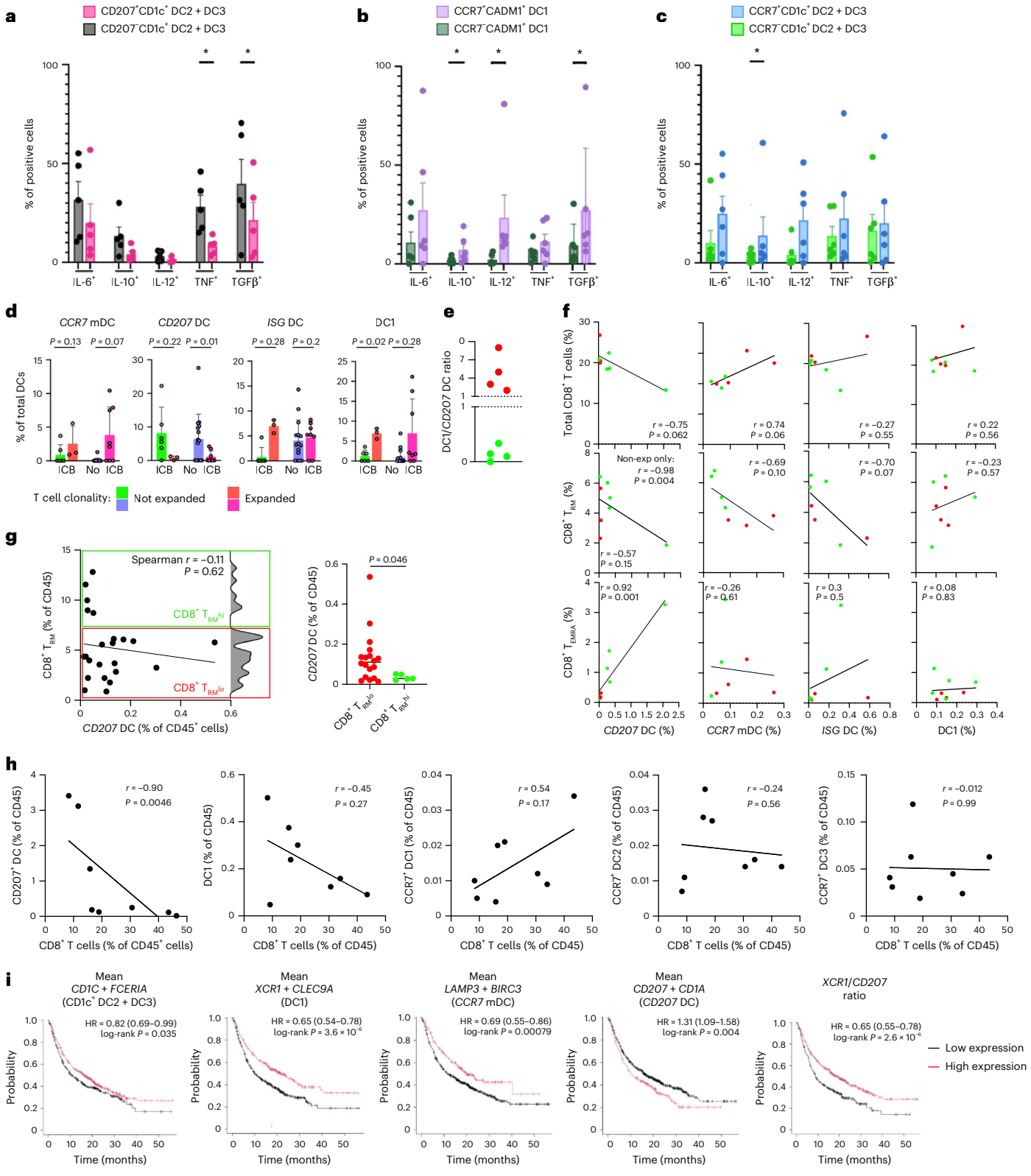

total CD8$^+$ T cells[45]. This revealed that *CD207* DCs exhibited a negative correlation with the frequency of *CD8* T cells and showed a significant inverse correlation with *CD8* T_{RM} cells (Fig. 7f), specifically in patients without T cell clonal expansion. This observation was extended to lung tumor scRNA-seq data[23], where the percentage of *CD207* DCs, but not that of the other DC populations, tended to be higher in patients with a low frequency of *CD8* T_{RM} cells (Fig. 7g and Extended Data Fig. 9d). We also observed a significant positive correlation between the frequencies of DC1s and *CD8* T_{RM} cells (Extended Data Fig. 9d). Additionally, within the breast cancer dataset[45], *CD207* DCs strongly correlated with T_{EMRA} cells, which are terminally differentiated, senescent and hypofunctional cells (Fig. 7f). Reanalyzing our flow cytometry data from patients with NSCLC, we also observed that the frequencies of CD207$^+$ DCs significantly negatively correlated with those of CD8$^+$ T cells, but not with those of CD4$^+$ T cells, while no correlation was observed between the other DC populations and T cell subsets (Fig. 7h and Extended Data Fig. 9e).

To confirm these observations in other datasets, we analyzed bulk RNA-seq data from patients with breast carcinoma (BRCA cohort) and those with lung adenocarcinoma (LUAD cohort), obtained from The Cancer Genome Atlas (TCGA) program (Extended Data Fig. 9f and Supplementary Table 1). We applied DC population signatures obtained from the mDC-VERSE, while other signatures were from published studies[46]. In both the BRCA and LUAD cohorts, among all mDC signatures, the *CD207* DC signature exhibited the most negative correlation with T cell subset signatures (*CD8* T cells, *CD8* T_{RM} cells and exhausted T cells for both cohorts; T_{reg} cells for the LUAD cohort alone) as well as with the DC1 signature (Extended Data Fig. 9f). Furthermore, among the different T cell subsets, the *CD8* T_{RM} signature demonstrated the most negative correlation with the *CD207* DC signature (Extended Data Fig. 9f).

Finally, we further explored cohorts of patients whose tumors were sampled and analyzed by bulk RNA-seq before receiving ICB treatment[47], to evaluate the prognostic value when using the gene signatures of major DC populations (Fig. 7i and Extended Data Fig. 9g). While the mean expression of the total CD1c$^+$ mDC (*CD1C*, *FCERIA*), DC1 (*XCR1*, *CLEC9A*) and *CCR7* mDC (*LAMP3*, *BIRC3*) gene signatures correlated with a statistically significant increase in overall survival, the mean expression of the *CD207* DC (*CD207*, *CD1A*) gene signature was associated with a statistically significant decrease in overall survival following ICB treatment (Fig. 7i and Extended Data Fig. 9g). There was also a statistically significant increase in overall survival when individual defining genes for each DC population (*XCR1*/*CADM1*/*CLEC9A* for DC1, *LAMP3*/*BIRC3*/*MARCKS* for *CCR7* mDCs, and *CD1C*, a pan-DC gene) were analyzed (Fig. 7i and Extended Data Fig. 9g). As the mean *CD1C* + *FCERIA* signature and the *CD1C* pan-CD1c$^+$ mDC (DC2 + DC3) gene were significantly associated with increased overall survival, this analysis indicated that the *CD207* state of DCs could be specifically associated with poor prognosis (Fig. 7i and Extended Data Fig. 9g). Notably, the DC1/*CD207* DC ratio (*XCR1*/*CD207*) was predictive of patient survival (Fig. 7i), consistent with the observations made regarding the expansion of T cell clonality (Fig. 7e). Altogether, the results of this analysis suggest that patients with low *CD207* DC and high DC1 and *CCR7* mDC tumor infiltrates respond better to ICB treatment and vice versa.

Discussion

Here, we provide an integrated analysis across multiple tissues in various cancers to create an in-depth overview of human DC heterogeneity. Using 40 scRNA-seq datasets, along with flow cytometry, CITE-seq, spatial transcriptomics, IHF and multiple analytical pipelines, we define a robust characterization of human DCs. The DC-VERSE enabled the mapping of all DCs from any scRNA-seq dataset, while the mDC-VERSE refined mDC classification and distinguished stressed cells, low-viability cells, B cell contaminants and T cell doublets. By integrating transcriptome data with protein data (CITE-seq, indexed FACS), the mDC-VERSE resolved discrete DC subsets and shared states between DC2s and DC3s. As such, CITE-seq data[18] allowed for the confirmed identification of DC2s/DC3s through CD5/CD14 and revealed CD103 expression on *LTB* and *CD207* DCs, validated by flow cytometry.

Our framework clarified the cDC2A_Brown and cDC2B_Brown clusters, separating *LTB* DCs, CD5$^+$ DC2s, and DC3s[30]. At the same time, we reinterpreted the previously defined 'CD1A DC2' cluster as *LTB* and *CD207* DCs[31]. It also detected rare RORγt$^+$ tolerogenic DCs[27,28] (<1% of DCs), a distinguished LC-like state, highlighting the power of reduced-variance analyses. Within the DC-VERSE, LC-like DCs also included *CD207* DCs that accumulated in tumors and *LTB* DCs that did not. These two cell states could only be defined when we analyzed mDCs (mDC-VERSE) alone, indicating that reducing the global variance of the dataset by analyzing less heterogeneous cells makes it possible to define discrete cell subsets and states.

The proliferation of scRNA-seq studies has led to variability in DC nomenclature, necessitating a unified terminology. DC3s were initially proposed as a subset of CD1c$^+$ DCs harboring proinflammatory CD14$^+$ cells[9,11]. Despite this, the term 'DC3' has also been used to describe cells[15,34,35] that have a transcriptomic alignment to *CCR7* mDCs[15,18,20]. Consequently, using the term 'DC3' to describe these two fundamentally different populations can be confusing for researchers, especially because CD5$^-$CD14$^{+/-}$ DC3s correspond to a cell subset, while *CCR7* mDCs represent a state shared by DC1, DC2s and DC3s[14]. The mDC-VERSE aligns these signatures from multiple studies, demonstrating that *CCR7* mDCs correspond to an activated and migratory state rather than a distinct subset. To evaluate the contamination of monocyte-derived DCs, we compared our data with a gene signature derived from in vitro-stimulated monocytes. The results showed that DC3s were the most similar to this monocyte signature. While the overlap was smaller than that observed in true monocytes and macrophages, monocyte contamination cannot be ruled out.

Understanding the difference between a subset and a state is crucial, especially when translating these findings into therapeutic strategies. The distinction can have a significant impact on the timing and location of targeted interventions, influencing the effectiveness of modulating immune responses. We focused on mDC heterogeneity between juxtatumoral and tumor tissues, as we had only limited access to clinical data, such as tumor features, aggressiveness or metastasis.

By comparing tumor and juxtatumoral tissues, we found *SPP1* upregulation and *CLEC9A* downregulation, indicating reduced DC1 density in tumors[38]. This was in contrast to the state of CCR7$^+$ DC1s, whose frequency, as evaluated by flow cytometry, was increased, highlighting that the states of subsets can increase independently. *ISG* DCs were also enriched in tumors, consistent with findings of antitumor *ISG* DC2s in mice[48]. While extending the expansion of *CCR7* mDCs and DC3s in multiple cancers[18,23], we functionally observed that CCR7$^+$ DC1s displayed elevated levels of IL-12 and costimulatory molecules, reinforcing their role as activated DCs[49]. In contrast, IL-10 upregulation was confined to CD1c$^+$ DCs[50].

Among the most notable findings was the characterization of *CD207* DCs, a tumor-associated state shared by DC2s and DC3s. Previous studies had already highlighted CD207 expression in tumor DCs, but their precise identity and localization remained unclear[19,23]. Using the mDC-VERSE, flow cytometry validation and IHF, we demonstrated that *CD207* DCs accumulate specifically within tumor nests, unlike other DCs, which are primarily enriched in the stroma. Transcriptomic data further showed the activation of HIF1α signaling, consistent with adaptation to hypoxia in the tumor core. Functionally, CD207$^+$ DCs exhibited a noticeably diminished capacity to produce key cytokines, with significant reductions in TGFβ and TNF secretion, as well as lower levels of IL-6 and IL-10. This impaired cytokine profile may have dual consequences for tumor immunity. On the one hand, reduced IL-6 and TGFβ levels could dampen T helper 17 (T_H17) cell differentiation and cytokine release (IL-17, IL-21, interferon-γ (IFNγ)), thereby limiting effective antitumor T cell responses[51]. Lower TNF levels could also

decrease local inflammation, blunting T cell recruitment and activation and favoring tumor immune evasion[52]. On the other hand, reduced IL-6 and TNF levels might constrain protumoral mechanisms such as angiogenesis, immunosuppressive macrophage activity and STAT3-mediated tumor progression[51]. In this way, CD207$^+$ DCs may occupy a paradoxical position in the tumor microenvironment, suppressing both protective and pathological immune processes.

The clinical relevance of CD207$^+$ DCs emerged most clearly in the context of immunotherapy. In ICB-treated patients, *CD207* DCs correlated negatively with T cell clonal expansion, which was associated with survival, in contrast to DC1s and *CCR7* mDCs. They also showed an inverse relationship with CD8$^+$ T_{RM} cells, which are associated with improved outcomes[53], and a positive correlation with dysfunctional T_{EMRA} cells[54]. Together, these findings suggest that CD207$^+$ DCs may actively skew CD8$^+$ T cell differentiation toward dysfunctional states, raising the possibility of targeting this subset to improve responses. Their inverse correlation with CD8$^+$ T_{RM} cells and positive correlation with dysfunctional T_{EMRA} cells may be explained by two, not mutually exclusive, hypotheses: competition with T cells for TGFβ, which leads to impaired T_{RM} differentiation, and the promotion of CD8$^+$ T cell progression toward a T_{EMRA} fate. These models provide a mechanistic rationale for why CD207$^+$ DCs correlate with poor survival and limited T cell clonality, underscoring the importance of further investigating this population as both a prognostic marker and a potential therapeutic target.

The DC-VERSE and mDC-VERSE were generated by integrating available single-cell datasets, which inherently limit the accurate estimation of absolute cell numbers. Therefore, observed population changes should be interpreted with caution and ideally confirmed by orthogonal approaches such as flow cytometry. Because the analysis was based on datasets available at the time, the inclusion of more recent data across additional cancer types and diseases could further strengthen the resource. Nonetheless, the multimodal reference mapping framework allows these VERSEs to serve as reference maps for querying new datasets as they emerge.

The functional analysis of CD207$^+$ DCs was restricted by the limited availability of fresh tumor samples, which reduced the ability to distinguish between DC2 and DC3 states and necessitated large tumor material to capture sufficient CD207$^+$ DCs for downstream assays. Given their rarity, larger patient cohorts and complementary strategies will be essential to validate the functional roles and clinical associations of CD207$^+$ DCs, including their correlation with T cell clonality, which was observed in a single dataset.

In summary, our study offers a comprehensive analysis of human DC heterogeneity, integrating diverse datasets and techniques to elucidate their roles in health and disease. The DC-VERSE and mDC-VERSE platforms provide valuable resources for researchers, enabling a deeper understanding of DCs and their implications for immunotherapy strategies. By providing an online tool for exploration, unifying nomenclature and shedding light on the spatial distribution and potential prognostic significance of specific DC subsets, our study paves the way for further research and targeted therapeutic interventions in the realm of DC biology.

Online content

Any methods, additional references, Nature Portfolio reporting summaries, source data, extended data, supplementary information, acknowledgements, peer review information; details of author contributions and competing interests; and statements of data and code availability are available at https://doi.org/10.1038/s41590-025-02337-x.

References

1. Steinman, R. M. & Cohn, Z. A. Identification of a novel cell type in peripheral lymphoid organs of mice: I. Morphology, quantitation, tissue distribution. *J. Exp. Med.* **137**, 1142–1162 (1973).
2. Nussenzweig, M. C., Steinman, R. M., Gutchinov, B. & Cohn, Z. A. Dendritic cells are accessory cells for the development of anti-trinitrophenyl cytotoxic T lymphocytes. *J. Exp. Med.* **152**, 1070–1084 (1980).
3. Steinman, R. M. & Witmer, M. D. Lymphoid dendritic cells are potent stimulators of the primary mixed leukocyte reaction in mice. *Proc. Natl Acad. Sci. USA* **75**, 5132–5136 (1978).
4. Steinman, R. M., Gutchinov, B., Witmer, M. D. & Nussenzweig, M. C. Dendritic cells are the principal stimulators of the primary mixed leukocyte reaction in mice. *J. Exp. Med.* **157**, 613–627 (1983).
5. Guilliams, M. et al. Dendritic cells, monocytes and macrophages: a unified nomenclature based on ontogeny. *Nat. Rev. Immunol.* **14**, 571–578 (2014).
6. Lee, J. et al. Restricted dendritic cell and monocyte progenitors in human cord blood and bone marrow. *J. Exp. Med.* **212**, 385–399 (2015).
7. Liu, K. et al. In vivo analysis of dendritic cell development and homeostasis. *Science* **324**, 392–397 (2009).
8. Naik, S. H. et al. Development of plasmacytoid and conventional dendritic cell subtypes from single precursor cells derived in vitro and in vivo. *Nat. Immunol.* **8**, 1217–1226 (2007).
9. Bourdely, P. et al. Transcriptional and functional analysis of CD1c$^+$ human dendritic cells identifies a CD163$^+$ subset priming CD8$^+$CD103$^+$ T cells. *Immunity* **53**, 335–352 (2020).
10. Cytlak, U. et al. Differential IRF8 transcription factor requirement defines two pathways of dendritic cell development in humans. *Immunity* **53**, 353–370.e8 (2020).
11. Dutertre, C.-A. et al. Single-cell analysis of human mononuclear phagocytes reveals subset-defining markers and identifies circulating inflammatory dendritic cells. *Immunity* **51**, 573–589 (2019).
12. See, P. et al. Mapping the human DC lineage through the integration of high-dimensional techniques. *Science* **356**, eaag3009 (2017).
13. Villani, A.-C. et al. Single-cell RNA-seq reveals new types of human blood dendritic cells, monocytes, and progenitors. *Science* **356**, eaah4573 (2017).
14. Ginhoux, F., Guilliams, M. & Merad, M. Expanding dendritic cell nomenclature in the single-cell era. *Nat. Rev. Immunol.* **22**, 67–68 (2022).
15. Di Pilato, M. et al. CXCR6 positions cytotoxic T cells to receive critical survival signals in the tumor microenvironment. *Cell* **184**, 4512–4530 (2021).
16. Lee, C. Y. C. et al. Tumour-retained activated CCR7$^+$ dendritic cells are heterogeneous and regulate local anti-tumour cytolytic activity. *Nat. Commun.* **15**, 682 (2024).
17. Magen, A. et al. Intratumoral dendritic cell–CD4$^+$ T helper cell niches enable CD8$^+$ T cell differentiation following PD-1 blockade in hepatocellular carcinoma. *Nat. Med.* **29**, 1389–1399 (2023).
18. Maier, B. et al. A conserved dendritic-cell regulatory program limits antitumour immunity. *Nature* **580**, 257–262 (2020).
19. Moon, C. Y. et al. Dendritic cell maturation in cancer. *Nat. Rev. Cancer* **25**, 225–248 (2025).
20. Zheng, C. et al. Landscape of infiltrating T cells in liver cancer revealed by single-cell sequencing. *Cell* **169**, 1342–1356 (2017).
21. Bell, D. et al. In breast carcinoma tissue, immature dendritic cells reside within the tumor, whereas mature dendritic cells are located in peritumoral areas. *J. Exp. Med.* **190**, 1417–1426 (1999).
22. Franken, A. et al. CD4$^+$ T cell activation distinguishes response to anti-PD-L1+anti-CTLA4 therapy from anti-PD-L1 monotherapy. *Immunity* https://doi.org/10.1016/j.immuni.2024.02.007 (2024).
23. Leader, A. M. et al. Single-cell analysis of human non-small cell lung cancer lesions refines tumor classification and patient stratification. *Cancer Cell* **39**, 1594–1609 (2021).

24. Zhang, Y. et al. Single-cell analyses reveal key immune cell subsets associated with response to PD-L1 blockade in triple-negative breast cancer. *Cancer Cell* **39**, 1578–1593 (2021).
25. Mulder, K. et al. Cross-tissue single-cell landscape of human monocytes and macrophages in health and disease. *Immunity* **54**, 1883–1900 (2021).
26. Levine, J. H. et al. Data-driven phenotypic dissection of AML reveals progenitor-like cells that correlate with prognosis. *Cell* **162**, 184–197 (2015).
27. Narasimhan, H. et al. RORγt-expressing dendritic cells are functionally versatile and evolutionarily conserved antigen-presenting cells. *Proc. Natl Acad. Sci. USA* **122**, e2417308122 (2025).
28. Rodrigues, P. F. et al. Rorγt-positive dendritic cells are required for the induction of peripheral regulatory T cells in response to oral antigens. *Cell* **188**, 2720–2737 (2025).
29. Gao, Y. et al. Single-cell analysis reveals the heterogeneity of monocyte-derived and peripheral type-2 conventional dendritic cells. *J. Immunol.* **207**, 837–848 (2021).
30. Brown, C. C. et al. Transcriptional basis of mouse and human dendritic cell heterogeneity. *Cell* **179**, 846–863 (2019).
31. Cheng, S. et al. A pan-cancer single-cell transcriptional atlas of tumor infiltrating myeloid cells. *Cell* **184**, 792–809 (2021).
32. Hao, Y. et al. Integrated analysis of multimodal single-cell data. *Cell* **184**, 3573–3587 (2021).
33. Cillo, A. R. et al. Immune landscape of viral- and carcinogen-driven head and neck cancer. *Immunity* **52**, 183–199 (2020).
34. Gerhard, G. M., Bill, R., Messemaker, M., Klein, A. M. & Pittet, M. J. Tumor-infiltrating dendritic cell states are conserved across solid human cancers. *J. Exp. Med.* **218**, e20200264 (2021).
35. Zilionis, R. et al. Single-cell transcriptomics of human and mouse lung cancers reveals conserved myeloid populations across individuals and species. *Immunity* https://doi.org/10.1016/j.immuni.2019.03.009 (2019).
36. Qian, J. et al. A pan-cancer blueprint of the heterogeneous tumor microenvironment revealed by single-cell profiling. *Cell Res.* **30**, 745–762 (2020).
37. Zhang, Q. et al. Landscape and dynamics of single immune cells in hepatocellular carcinoma. *Cell* **179**, 829–845 (2019).
38. Kvedaraite, E. & Ginhoux, F. Human dendritic cells in cancer. *Sci. Immunol.* **7**, eabm9409 (2022).
39. Merad, M., Sathe, P., Helft, J., Miller, J. & Mortha, A. The dendritic cell lineage: ontogeny and function of dendritic cells and their subsets in the steady state and the inflamed setting. *Annu. Rev. Immunol.* https://doi.org/10.1146/annurev-immunol-020711-074950 (2013).
40. Hao, Y. et al. Dictionary learning for integrative, multimodal and scalable single-cell analysis. *Nat. Biotechnol.* **42**, 293–304 (2024).
41. Lamb, J. et al. The Connectivity Map: using gene-expression signatures to connect small molecules, genes, and disease. *Science* **313**, 1929–1935 (2006).
42. Kvedaraite, E. et al. Notch-dependent cooperativity between myeloid lineages promotes Langerhans cell histiocytosis pathology. *Sci. Immunol.* **7**, eadd3330 (2022).
43. Bigley, V. et al. Langerin-expressing dendritic cells in human tissues are related to CD1c$^+$ dendritic cells and distinct from Langerhans cells and CD141^{high} XCR1$^+$ dendritic cells. *J. Leukoc. Biol.* **97**, 627–634 (2015).
44. Wu, S. Z. et al. A single-cell and spatially resolved atlas of human breast cancers. *Nat. Genet.* **53**, 1334–1347 (2021).
45. Bassez, A. et al. A single-cell map of intratumoral changes during anti-PD1 treatment of patients with breast cancer. *Nat. Med.* **27**, 820–832 (2021).
46. Ramos, R. N. et al. Tissue-resident FOLR2$^+$ macrophages associate with CD8$^+$ T cell infiltration in human breast cancer. *Cell* **185**, 1189–1207 (2022).
47. Lánczky, A. & Győrffy, B. Web-based survival analysis tool tailored for medical research (KMplot): development and implementation. *J. Med. Internet Res.* **23**, e27633 (2021).
48. Duong, E. et al. Type I interferon activates MHC class I-dressed CD11b$^+$ conventional dendritic cells to promote protective anti-tumor CD8$^+$ T cell immunity. *Immunity* https://doi.org/10.1016/j.immuni.2021.10.020 (2021).
49. Garris, C. S. et al. Successful anti-PD-1 cancer immunotherapy requires T cell–dendritic cell crosstalk involving the cytokines IFN-γ and IL-12. *Immunity* **49**, 1148–1161 (2018).
50. Gabrilovich, D. Mechanisms and functional significance of tumour-induced dendritic-cell defects. *Nat. Rev. Immunol.* **4**, 941–952 (2004).
51. Caetano, M. S. et al. IL6 blockade reprograms the lung tumor microenvironment to limit the development and progression of K-ras-mutant lung cancer. *Cancer Res.* **76**, 3189–3199 (2016).
52. Liu, Z. et al. Duality of interactions between TGF-β and TNF-α during tumor formation. *Front. Immunol.* **12**, 810286 (2022).
53. Park, S. L., Gebhardt, T. & Mackay, L. K. Tissue-resident memory T cells in cancer immunosurveillance. *Trends Immunol.* **40**, 735–747 (2019).
54. Reading, J. L. et al. The function and dysfunction of memory CD8$^+$ T cells in tumor immunity. *Immunol. Rev.* **283**, 194–212 (2018).

[1]INSERM U1015, Gustave Roussy, Paris-Saclay University, Villejuif, France. [2]Centre de Recherche des Cordeliers, INSERM, Sorbonne Université, USPC Université Paris Cité, Equipe Labellisée Ligue Nationale Contre le Cancer, Paris, France. [3]Faculté de Santé, Université Paris Cité, Paris, France. [4]Immunobiology Laboratory, The Francis Crick Institute, London, UK. [5]INSERM U981, PRISM Center, Gustave Roussy, Paris-Saclay University, Villejuif, France. [6]Laboratory of Mathematics and Computer Science (MICS), CentraleSupélec, Paris-Saclay University, Gif-sur-Yvette, France. [7]Vizgen, Cambridge, MA, USA. [8]Broad Institute of MIT and Harvard, Cambridge, MA, USA. [9]Cancer Ecosystems Program, Garvan Institute of Medical Research, Darlinghurst, New South Wales, Australia. [10]School of Clinical Medicine, Faculty of Medicine & Health, UNSW Sydney, Sydney, New South Wales, Australia. [11]INSERM U1186, Gustave Roussy, Paris-Saclay University, Villejuif, France. [12]Institute of Systems Immunology, Hamburg Center for Translational Immunology (HCTI), University Medical Center Hamburg-Eppendorf, Hamburg, Germany. [13]Plateforme de Bioinformatique, INSERM US23, CNRS UMS 3655, Université Paris-Saclay, Villejuif, France. [14]Program in Emerging Infectious Disease, Duke-NUS Medical School, Singapore, Singapore. [15]Pathology Department, Marie Lannelongue Center, Le Plessis Robinson, France. [16]Singapore Immunology Network (SIgN), A*STAR, Singapore, Singapore. [17]Shanghai Institute of Immunology, Shanghai Jiao Tong University School of Medicine, Shanghai, China. [18]Present address: INSERM U955, Institut Mondor de Recherche Biomédicale (IMRB), Université Paris-Est Créteil, Créteil, France. [19]These authors contributed equally: Kevin Mulder, Margaux Gardet. [20]These authors jointly supervised this work: Florent Ginhoux, Charles-Antoine Dutertre. ✉e-mail: Florent_Ginhoux@a-star.edu.sg; charles-antoine.dutertre@inserm.fr

Methods

Human tissue and blood samples

Tumor and juxtatumoral tissues from the lung, as well as FFPE blocks, were obtained from patients with NSCLC ($n = 8$) following written informed consent (Marie Lannelongue Hospital, Paris) and ethical approval (No. ID-RCB: 2016-A00732-49). All patients provided institutional review board-approved consent. Human tissues were cut into 0.5-cm squares and incubated with 0.8 mg ml^{-1} collagenase (type IV, Worthington Biochemical) in RPMI (PAA) with 10% fetal calf serum (FCS) (Autogen Bioclear) for 2 and 8 h, respectively, or when stated, mechanically dispersed.

Flow cytometry

For the NSCLC juxtatumoral and tumor samples, cells were thawed and transferred into RPMI (Thermo Fisher) with 20% decomplemented FCS (Thermo Fisher). Samples were treated with 1 mg ml^{-1} DNase I (Sigma-Aldrich) at 37 °C. Cells were incubated with Live/Dead Blue dye (Invitrogen) for 30 min at 4 °C in PBS and then incubated in 5% heat-inactivated FCS (Sigma-Aldrich) for 15 min at 4 °C. Cells were stained with appropriate antibodies in PBS containing 2% FCS, 2 mM EDTA (Sigma-Aldrich) and Brilliant Stain buffer (BD). The cells were then incubated for 30 min at 4 °C and washed. Samples were analyzed on a Cytek Aurora five-laser spectral analyzer. Flow cytometry files were exported and analyzed using FlowJo v10.8.1.

IHF labeling assays

All immunostainings were performed on 4-µm FFPE whole sections from human NSCLC samples (Marie Lannelongue Hospital, Paris). Antigen retrieval was carried out on a PT-Link (Dako) using EnVision FLEX target retrieval solutions at high pH (Dako, K8004) or low pH (Dako, K8005). Endogenous peroxidase activity and nonspecific Fc receptor binding were blocked with 3% H_2O_2 (Gilbert, 3518646067907) and Protein Block (Dako, X0909), respectively. Necrotic, serous, folded and blurred areas were excluded from the analyses. The CD20/CD3/CD207/CD8 four-plex staining was performed manually using the OPAL tyramide system amplification (TSA) system (Akoya Biosciences). Nuclei were stained with DAPI (Thermo Fisher, 62248) at 2 µg ml^{-1} for 5 min. Slides were mounted with ProLong Glass Antifade (Thermo Fisher, P36980) and scanned at 20× on a Zeiss Axio Scan Z1. The primary antibodies, secondary antibodies and TSA kits used are listed in the key resources table.

Functional DC assay

Lung tumor samples from five patients were processed into a single-cell suspension. Cells were counted and cultured at 3 million in a 96-well plate (Falcon, 353077) in RPMI 1640 (Gibco, 11875-093), supplemented with 10% FBS (charcoal-stripped; Merck, F6765), 1% penicillin–streptomycin (Gibco, 15144-122), 1% sodium pyruvate (Gibco, 11360-070), 1% HEPES (Gibco, 15630-056) and 0.1% 2-mercaptoethanol (Gibco, 21985-023) at 37 °C and 5% CO_2 for 3 h. Brefeldin A (Invitrogen, 00-4506-51) was added to the solution. Cell yields varied with sample size, resulting in different replicate numbers for each stimulation condition (unstimulated condition, $n = 5$). After overnight stimulation, cells were washed in PBS, stained with antibodies (Supplementary Table 1) in FACS stain buffer (BD, 554656) and Brilliant Stain buffer (BD, 563794) at room temperature for 15 min, washed, and permeabilized using the FOXP3/Transcription Factor Fixation/Permeabilization Kit (Invitrogen 00-5521-00) for 20 min at 4 °C. Cytokine antibodies (TNF, TGFβ, IL-6, IL-10, IFNγ, IL12p40/p70) were added for 20 min at 4 °C in permeabilization buffer solution. Cells were analyzed using a Cytek Aurora five-laser spectral analyzer. Flow cytometry files were analyzed with FlowJo v10.8.1.

Cell sorting of tumor DCs for bulk RNA-seq

Ovarian tumor cells were digested with collagenase (1 mg ml^{-1}, Sigma C5138-IG) and DNase (0.1 mg ml^{-1}, Roche, 11 284 932 001) for 30 min at 37 °C and centrifuged at 100 rpm. The cells were then passed through a 16G needle and a 70-µm strainer to disrupt the tissue. Cells were washed and stained with Live/Dead Blue dye (Invitrogen, L23105) for 20 min at 4 °C in PBS. To block Live/Dead Blue dye, cells were resuspended in PBS containing 20% FBS for 15 min at 4 °C.

Cells were incubated in FACS buffer for 30 min at 4 °C with an optimized concentration of the primary antibodies (Supplementary Table 1) in FACS stain buffer (BD, 554656) and Brilliant Stain buffer (BD, 563794). Following staining with primary antibodies, the cells were washed and then stained with anti-chicken Alexa Fluor 647 secondary antibody for 20 min at 4 °C. After washing, the cells were resuspended in RPMI with 10% FBS, filtered through a 40-µm strainer and sorted. Up to 350 CD207$^+$ DC and CD207$^-$ DC2/DC3 subsets were isolated (>95% purity) using a FACSAria II Fusion sorter (BD Biosciences), directly into 1× lysis buffer (Takara, 635013) for ultralow-input bulk RNA-seq lysis, and stored at −80 °C.

Bulk RNA-seq, ultralow input

Sequencing libraries of the sorted cells were prepared using the SMART-Seq mRNA LP kit (Takara Bio). cDNA synthesis was performed according to the manufacturer's instructions and assessed using a high-sensitivity Bioanalyzer chip (Agilent Technologies). Library preparation followed the standard protocol, except for the final purification, which was replaced by size selection using AMPure XP beads (0.8–0.6×). Some samples underwent cDNA reamplification to increase yield. Libraries were pooled in equimolar proportions and sequenced on a NextSeq 2000 system (Illumina) using a P3 paired-end 2 × 55 bp run. Demultiplexing was performed using bcl-convert 4.1.5. Adaptor sequences were trimmed with Cutadapt 3.2, and only reads exceeding 10 bp were retained for downstream analysis.

Algorithms for dimensionality reduction

Flow cytometry marker values were transformed using the automated logicle function from the flowCore R package. UMAP was carried out using all markers (flow cytometry) or significant PCs (based on Seurat analysis for scRNA-seq data). UMAP was run using 15 nearest neighbors, a minimum distance of 0.01 to 0.2 and Euclidean distance[55,56]. Phenograph clustering[26] was performed using all markers or significant PCs (based on Seurat analysis) before dimension reduction. The number of PCs selected was 50 for the DC-VERSE and the mDC-VERSE, 30 for flow cytometry and 15 for scRNA-seq analysis.

MNP extraction and integration

We previously integrated 41 datasets examining monocyte and macrophage heterogeneity[25]. Comparably, for DCs, 40 of 41 datasets were used (one was excluded due to low cell numbers; Supplementary Table 1)[11,13,18,20,25,30,33,35,44,57–78]. Datasets were either raw count matrices or preprocessed and filtered. Normalization depended on the technique used, such as 10x data or Smart-seq2 sequencing[11,25]. Integration of the datasets was performed as previously described[57–59,63,64,79,80].

Label transfer and multimodal reference mapping

For cell metadata transfer and multimodal reference mapping, we used the label transfer and multimodal reference mapping pipeline from Seurat[40,80]. The algorithm returns a prediction score for each class for every cell in the query dataset, and the cutoff score is set at 0.4.

Differentially expressed genes

DEG analyses were performed using the Seurat package. DEGs obtained from the 'RNA' matrix of the Seurat object were calculated based on normalized values with a log(fold change) threshold of 0.25 and a threshold for false discovery of 0.05. The likelihood ratio test for single-cell gene expression (bimodal test) was used, and correction for multiple testing was carried out using the Bonferroni method.

Dendrogram heatmap to define DC-VERSE and mDC-VERSE megaclusters

The average expression of each gene obtained from the DEG analysis for each Phenograph cluster was first determined, and the Spearman correlation was calculated. A dendrogram heatmap was then generated with pheatmap using Ward's method for hierarchical cluster analysis.

Published DC signature score heatmap

The signature score heatmap was generated using pheatmap, and signatures were obtained from various public datasets. The DC-VERSE and mDC-VERSE were divided into the defined megaclusters, and we obtained the average gene expression of every megacluster for all the genes present. Following this, the mean expression of the signature was calculated and plotted by the megaclusters in the heatmap.

Metadata analysis

Metadata analysis was performed on selected studies with paired conditions (juxtatumoral tissues versus tumors). The proportion of megaclusters was plotted for each state as charts and density plots for the selected studies. Further analysis was performed to deconvolute data at the patient level in datasets where this information was provided. We only analyzed datasets where more than eight cells were present. Charts and density plots were created using GraphPad Prism v6 and SeqGeq v1.6, respectively. Statistical tests were performed using GraphPad Prism and are specified in the figure legends.

SCENIC gene regulatory network analyses

Gene regulatory networks were inferred from transcripts per million-normalized lung[18] and head and neck[33] expression matrices using pySCENIC (v0.10.3)[47]. The workflow included the following (GitHub/pySCENIC): (1) coexpression module generation with GRNBoost2, (2) refinement with RcisTarget and (3) regulon activity evaluation with AUCell[81]. DERs were calculated using the Seurat pipeline with DEG parameters (adjusted $P \leq 0.05$, $\log_2$(fold change) ≥ 0.25). Phenograph cluster-specific DERs and DERs with similar expression patterns across related Phenograph clusters were then used to generate a heatmap.

Spatial transcriptomic analysis (Visium 10x Genomics)

The analysis was performed as previously described by Wu et al.[44]. Spatial transcriptomic Visium data were deconvoluted with Stereoscope 0.3.1 using the breast cancer scRNA-seq reference from Wu et al.[44]. Reference cells were filtered with the --sc_upper_bound option up to 1,000 per cell type (randomly selected). Genes were restricted to 3,695 highly variable genes, as identified using the sc.pp.highly_variable_genes function from Scanpy (Single-Cell Analysis in Python) with default parameters, and the --filter-genes option was also enabled. Model fitting and application were each run for 75,000 epochs with a batch size of 100. The pathology annotations from Wu et al.[44] were used to assess the enrichment of spatially deconvoluted subsets, and the deconvoluted proportion results were mapped onto H&E images using Seurat v4.

MERFISH analysis

Breast and lung cancer FFPE samples were processed following Vizgen's FFPE protocol using Vizgen's Cell Boundary Kit (10400009). The samples were then imaged on the MERSCOPE system (Vizgen, 10000001) using a 500-gene panel (Supplementary Table 1). Cell boundaries were defined using Cellpose[82] from the CLAHE-filtered DAPI and cell boundary 3 images merged with boundaries identified from only the CLAHE-filtered DAPI images. Segmentation was performed on the center *z* plane imaged on the MERSCOPE system and extrapolated across all seven *z* planes. Transcripts per boundary were tabulated to build a cell-by-gene matrix for clustering. MERSCOPE output data are available through Vizgen's data release program (https://info.vizgen.com/merscope-ffpe-solution). Following segmentation, a single-cell analysis was performed using the Scanpy library[83]. MERFISH data were filtered to remove cells with low counts or a low number of unique genes expressed (25 genes and 10 counts, respectively). Cells were normalized to equal total counts, and gene expression counts were log-transformed and scaled to unit variance. PCA, UMAP embedding (10 neighbors, 0.1 minimum distance and spread 3.0) and Leiden clustering (resolution of 1.5) were performed. Leiden clusters were manually annotated. PCA was performed on the immune and myeloid compartments, where PCs with strong loadings on immune-associated genes were selected for running UMAP embedding (15 neighbors, 0.01 minimum distance and spread 3.0) and Phenograph clustering (K50).

Pathway analysis

The DEGs of DC populations, along with the respective fold changes and *P* values, were uploaded to the IPA software (Qiagen). IPA analysis reported the *P* values of canonical pathways. Predicted upregulated or downregulated pathways were represented by positive or negative *z* scores, respectively. Canonical pathways determined by IPA's default threshold ($-\log(P\text{ value}) > 1.3$) were then shortlisted, and bubble plots were used to visualize the *P* values and *z* scores. Complete lists of pathways can be found in Supplementary Table 1.

Bulk RNA analysis

Differential expression analysis was conducted using DESeq2 (v1.38.1), with donor information incorporated as a covariate. Logarithmic fold changes were subsequently adjusted using the lfcShrink algorithm with the 'Ashr' option. The resulting signature of the *CD207* DCs was ranked and used for differential enrichment analysis under the predefined conditions.

TCGA analysis

Correlation matrices were generated using signatures from Mulder et al.[25], Ramos et al.[46] and Mackay et al.[84]. TCGA datasets were *z*-score-scaled per patient, and average signature values were calculated. Pearson correlations (*r*, two-tailed) were computed and plotted using the corrplot R package (v0.84).

Quantification and statistical analysis of IHF labeling

Tumor and juxtatumoral tissue areas were defined by a pathologist (G.G.). Tumors, nests and stroma were identified using Halo (Indica Labs) with a trained classifier. Cell density ($CD3^+$, $CD8^+$, $CD20^+$, $CD207^+$) was quantified in each zone using Halo counting algorithms.

Reporting summary

Further information on research design is available in the Nature Portfolio Reporting Summary linked to this article.

Data availability

No new data were generated; all analyzed datasets are public (Supplementary Table 1). The DC-VERSE and mDC-VERSE are available for download at https://github.com/gustaveroussy/FG-Lab.

Code availability

The DC-VERSE and the mDC-VERSE code can be found at https://github.com/gustaveroussy/FG-Lab.

References

55. Becht, E. et al. Dimensionality reduction for visualizing single-cell data using UMAP. *Nat. Biotechnol.* https://doi.org/10.1038/nbt.4314 (2018).
56. McInnes, L., Healy, J. & Melville, J. UMAP: uniform manifold approximation and projection for dimension reduction. Preprint at *arXiv* https://doi.org/10.48550/arXiv.1802.03426 (2018).
57. MacParland, S. A. et al. Single cell RNA sequencing of human liver reveals distinct intrahepatic macrophage populations. *Nat. Commun.* **9**, 4383 (2018).

58. Aizarani, N. et al. A human liver cell atlas reveals heterogeneity and epithelial progenitors. *Nature* **572**, 199–204 (2019).
59. Ramachandran, P. et al. Resolving the fibrotic niche of human liver cirrhosis at single-cell level. *Nature* **575**, 512–518 (2019).
60. Sharma, A. et al. Onco-fetal reprogramming of endothelial cells drives immunosuppressive macrophages in hepatocellular carcinoma. *Cell* **183**, 377–394 (2020).
61. Tang-Huau, T.-L. et al. Human in vivo-generated monocyte-derived dendritic cells and macrophages cross-present antigens through a vacuolar pathway. *Nat. Commun.* **9**, 2570 (2018).
62. Azizi, E. et al. Single-cell map of diverse immune phenotypes in the breast tumor microenvironment. *Cell* **174**, 1293–1308 (2018).
63. Kim, D. et al. Targeted therapy guided by single-cell transcriptomic analysis in drug-induced hypersensitivity syndrome: a case report. *Nat. Med.* **26**, 236–243 (2020).
64. Nakamizo, S. et al. Single-cell analysis of human skin identifies $CD14^+$ type 3 dendritic cells co-producing IL1B and IL23A in psoriasis. *J. Exp. Med.* **218**, e20202345 (2021).
65. Cheng, J. B. et al. Transcriptional programming of normal and inflamed human epidermis at single-cell resolution. *Cell Rep.* **25**, 871–883 (2018).
66. He, H. et al. Mild atopic dermatitis lacks systemic inflammation and shows reduced nonlesional skin abnormalities. *J. Allergy Clin. Immunol.* **147**, 1369–1380 (2021).
67. Xue, D., Tabib, T., Morse, C. & Lafyatis, R. Single-cell RNA sequencing reveals different subsets of macrophage and dendritic cells in human skin. *J. Immunol.* **202**, 177.8 (2019).
68. Smillie, C. S. et al. Intra- and inter-cellular rewiring of the human colon during ulcerative colitis. *Cell* **178**, 714–730 (2019).
69. Zhang, L. et al. Single-cell analyses inform mechanisms of myeloid-targeted therapies in colon cancer. *Cell* **181**, 442–459 (2020).
70. James, K. R. et al. Distinct microbial and immune niches of the human colon. *Nat. Immunol.* **21**, 343–353 (2020).
71. Lee, H.-O. et al. Lineage-dependent gene expression programs influence the immune landscape of colorectal cancer. *Nat. Genet.* **52**, 594–603 (2020).
72. Reyfman, P. A. et al. Single-cell transcriptomic analysis of human lung provides insights into the pathobiology of pulmonary fibrosis. *Am. J. Respir. Crit. Care Med.* **199**, 1517–1536 (2019).
73. Vieira Braga, F. A. et al. A cellular census of human lungs identifies novel cell states in health and in asthma. *Nat. Med.* **25**, 1153–1163 (2019).
74. Lambrechts, D. et al. Phenotype molding of stromal cells in the lung tumor microenvironment. *Nat. Med.* **24**, 1277–1289 (2018).
75. Kim, N. et al. Single-cell RNA sequencing demonstrates the molecular and cellular reprogramming of metastatic lung adenocarcinoma. *Nat. Commun.* **11**, 2285 (2020).
76. Arazi, A. et al. The immune cell landscape in kidneys of patients with lupus nephritis. *Nat. Immunol.* **20**, 902–914 (2019).
77. Stewart, B. J. et al. Spatiotemporal immune zonation of the human kidney. *Science* **365**, 1461–1466 (2019).
78. Peng, J. et al. Single-cell RNA-seq highlights intra-tumoral heterogeneity and malignant progression in pancreatic ductal adenocarcinoma. *Cell Res.* **29**, 725–738 (2019).
79. Becht, E. et al. Dimensionality reduction for visualizing single-cell data using UMAP. *Nat. Biotechnol.* **37**, 38–44 (2019).
80. Stuart, T. et al. Comprehensive integration of single-cell data. *Cell* **177**, 1888–1902 (2019).
81. Van de Sande, B. et al. A scalable SCENIC workflow for single-cell gene regulatory network analysis. *Nat. Protoc.* **15**, 2247–2276 (2020).
82. Stringer, C., Wang, T., Michaelos, M. & Pachitariu, M. Cellpose: a generalist algorithm for cellular segmentation. *Nat. Methods* **18**, 100–106 (2021).
83. Wolf, F. A., Angerer, P. & Theis, F. J. SCANPY: large-scale single-cell gene expression data analysis. *Genome Biol.* **19**, 15 (2018).
84. Mackay, L. K. et al. Hobit and Blimp1 instruct a universal transcriptional program of tissue residency in lymphocytes. *Science* **352**, 459–463 (2016).

Acknowledgements

We thank L. Robinson of Insight Editing London for the critical review and editing of the manuscript. We thank Y. Velut for providing the immunohistofluorescence images, as well as the Cell Imaging and Flow Cytometry Platform (CHIC) of the Centre de Recherche des Cordeliers for its help with this study. We thank the Foundation MSD Avenir (https://www.msdavenir.fr/) for its financial contribution to this project. We thank the Marie Lannelongue Hospital and its biobank for their valuable collaboration and support of this study. This work was supported by INSERM, Sorbonne Université, Université de Paris, Ligue Contre le Cancer (Equipe Labellisée), the CARPEM (Cancer Research for Personalized Medicine) program of the Sites Intégrés de Recherche sur le Cancer (SIRIC), and LabEx Immuno-Oncology. F.G. is an EMBO YIP awardee and is supported by Singapore Immunology Network (SIgN) core funding as well as a Singapore National Research Foundation Senior Investigatorship (NRFI) NRF2016NRF-NRFI001-02 and the Foundation Gustave Roussy. C.-A.D. is an INSERM researcher supported by INSERM. L.Z. was supported by the European Union's Horizon 2020 research and innovation program under grant agreement no. 825410 (ONCOBIOME project), ANR RHU5 'ANR-21-5 RHUS-0017' IMMUNOLIFE, MAdCAM INCA_16698 and ERC advanced, funded by the European Research Council (ERC) under grant agreement number 101052444, the ANR-23-RHUS-0010 (LUCA-pi), the European Union's Horizon 2020 research and innovation program no. 964590 (project acronym: IHMCSA, project title: International Human Microbiome Coordination and Support Action), the European Union's Horizon Europe research and innovation program under grant agreement no. 101095604 (project acronym: PREVALUNG EU, project title: Personalized lung cancer risk assessment leading to stratified interception), as well as by the SEERAVE Foundation. Other grant supports include Ligue Contre le Cancer and the SIGN'IT ARC Foundation (MICROBIONT-PREDICT, 2021).

Author contributions

Experiments: K.M., M.G. W.T.K., A.A.P., A.C., C.d.l.C.-F., E.P., L.R., A.B., S.K. and A.-G.G. Data analysis: K.M., M.G., W.T.K., A.A.P., A.C., G.G., C.d.l.C.-F., C.P., Q.B., E.L., A.-A.A., G.D., G.P., G.A.-E., R.J.D. and C.-A.D. Provision of human NSCLC samples: A.-G.G. and L.Z. Provision of human NSCLC FFPE blocks: V.T.d.M. Provision of human ovarian samples: C.d.l.C.-F. and J.M. Provision of breast cancer Visium spatial transcriptomic data: A.S. Generation, provision and segmentation of MERFISH data: L.H., T.W., J.H. and G.E. Establishment of the publicly available online DC-VERSE and mDC-VERSE: K.M. and M.D. Writing of the manuscript: K.M., M.G., W.T.K., A.A.P., F.G. and C.-A.D. Online cellXgene VERSEs: M.D. Intellectual input: C.S.-F., W.H.F. and A.B. Project supervision: F.G. and C.-A.D. Study conceptualization: F.G. and C.-A.D.

Competing interests

F.G. and C.-A.D. are coinventors of a patent related to the findings described in this article. The other authors declare no competing interests.

Additional information

Extended data is available for this paper at https://doi.org/10.1038/s41590-025-02337-x.

Supplementary information The online version contains supplementary material available at https://doi.org/10.1038/s41590-025-02337-x.

Correspondence and requests for materials should be addressed to Florent Ginhoux or Charles-Antoine Dutertre.

Peer review information *Nature Immunology* thanks the anonymous reviewers for their contribution to the peer review of this work.

Peer reviewer reports are available. Primary Handling Editor: Ioana Staicu, in collaboration with the *Nature Immunology* team.

https://doi.org/10.1038/s41590-025-02337-x

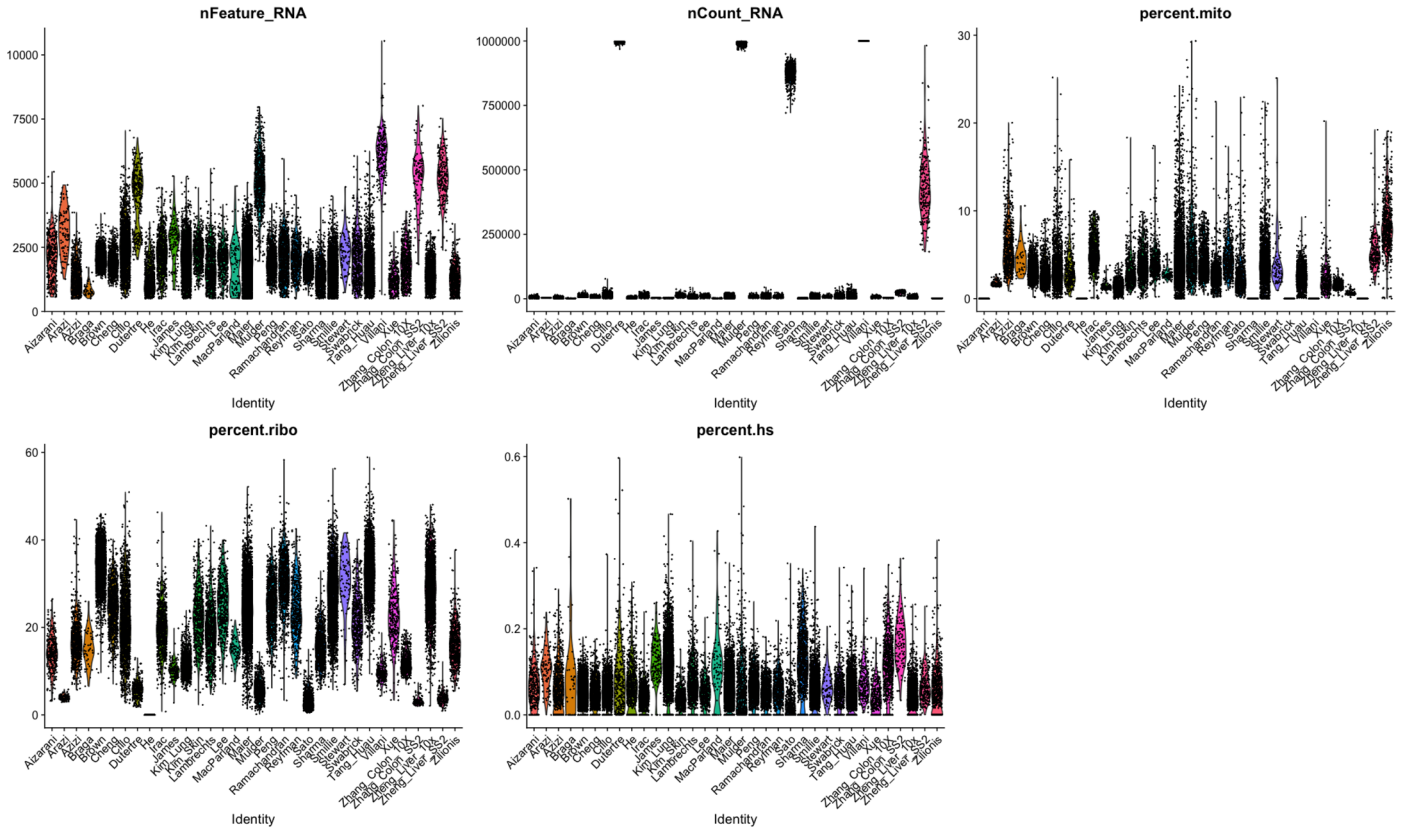

Extended Data Fig. 1 | Quality control plots of datasets included in the study. Violin plots displaying nFeature RNA, nCounts RNA, the percentage of mitochondrial genes (percent.mito), the percentage of ribosomal genes (percent.ribo), and the percentage of heat shock protein genes (percent.hs). Related to Fig. 1.

https://doi.org/10.1038/s41590-025-02337-x

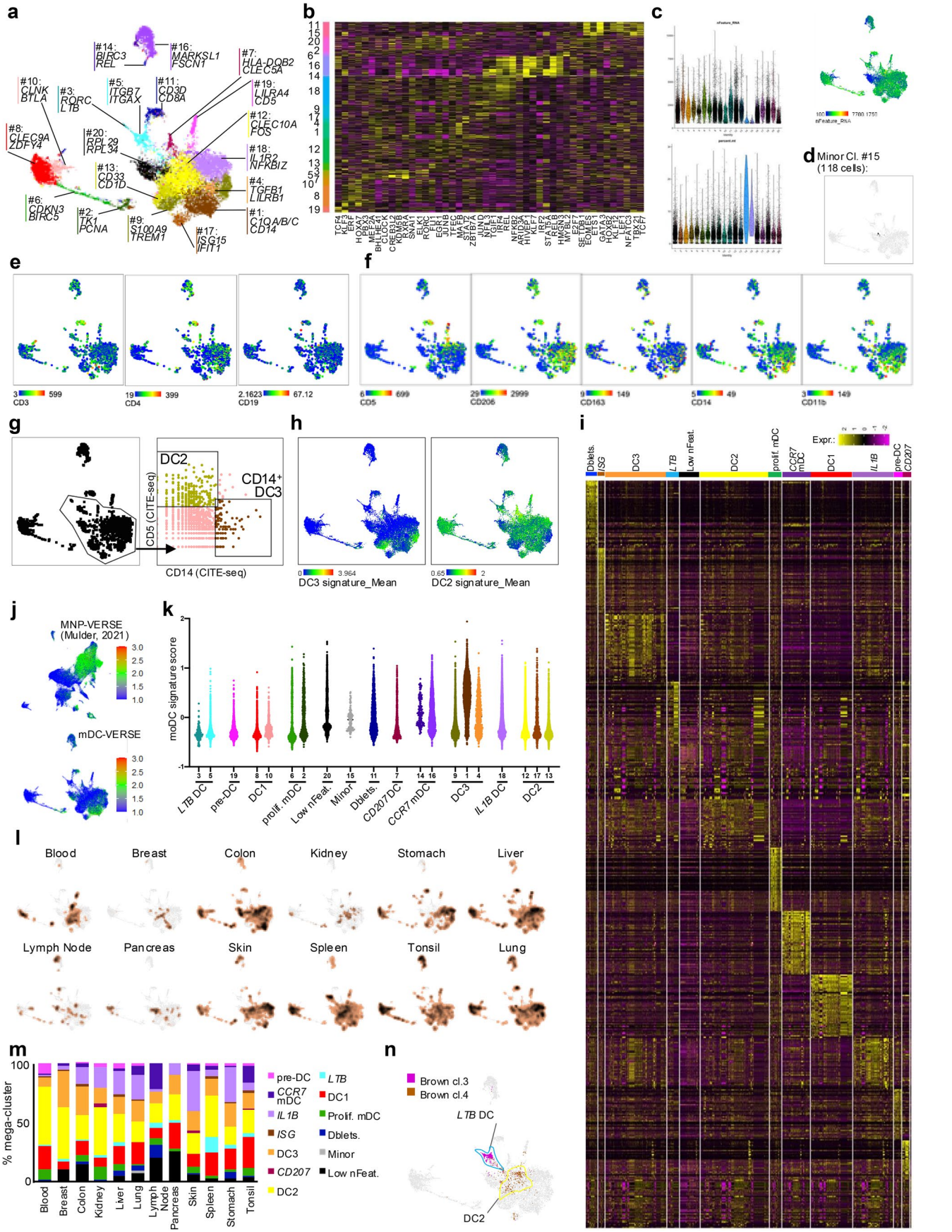

Extended Data Fig. 2 | See next page for caption.

https://doi.org/10.1038/s41590-025-02337-x

Extended Data Fig. 2 | Identification of clusters within the mDC-VERSE and mDC mega clusters' distribution across juxta-tumoral "healthy" tissues. **a**, Phenograph clusters' (cl.) annotation of the mDC-VERSE. **b**, Heatmap showing the relative expression levels of Differentially Expressed Regulons (DERs) between phenograph clusters common to Lung (Maier) and Tonsil (Cillo) cancer datasets. **c**, Quality control metrics for each Phenograph cluster and meaning plot of nFeature_RNA. **d**, Annotation of cl. #15 on the mDC-VERSE. **e-f**, CITE-seq data (from Maier et al.) showing expression of signature T and B cell protein markers and DC2 and DC3 protein markers. **g**, Identification of DC2s and DC3s using CD5 and CD14 protein expression from CITE-seq data (from Maier et al.) within the DC2 + DC3 region of the mDC-VERSE. **h**, Meaning plots of DC2 and DC3 gene signatures from Dutertre et al. on the mDC-VERSE. **i**, DEG heatmap between mega-clusters of the mDC-VERSE. **j**, Mean expression of the moDC signature from Gao et al. overlayed onto the MNP-VERSE (from Mulder et al.) and onto the mDC-VERSE UMAP spaces. **k**, moDC signature score for each cell of the different mDC-VERSE Phenograph clusters. **l,m**, Composition of DC mega clusters across juxta-tumoral "healthy" tissues. **n**, Annotation of cl.3 & cl.4 (corresponding to cDC2As_Brown) from Brown et al. on the mDC-VERSE. Related to Fig. 2.

https://doi.org/10.1038/s41590-025-02337-x

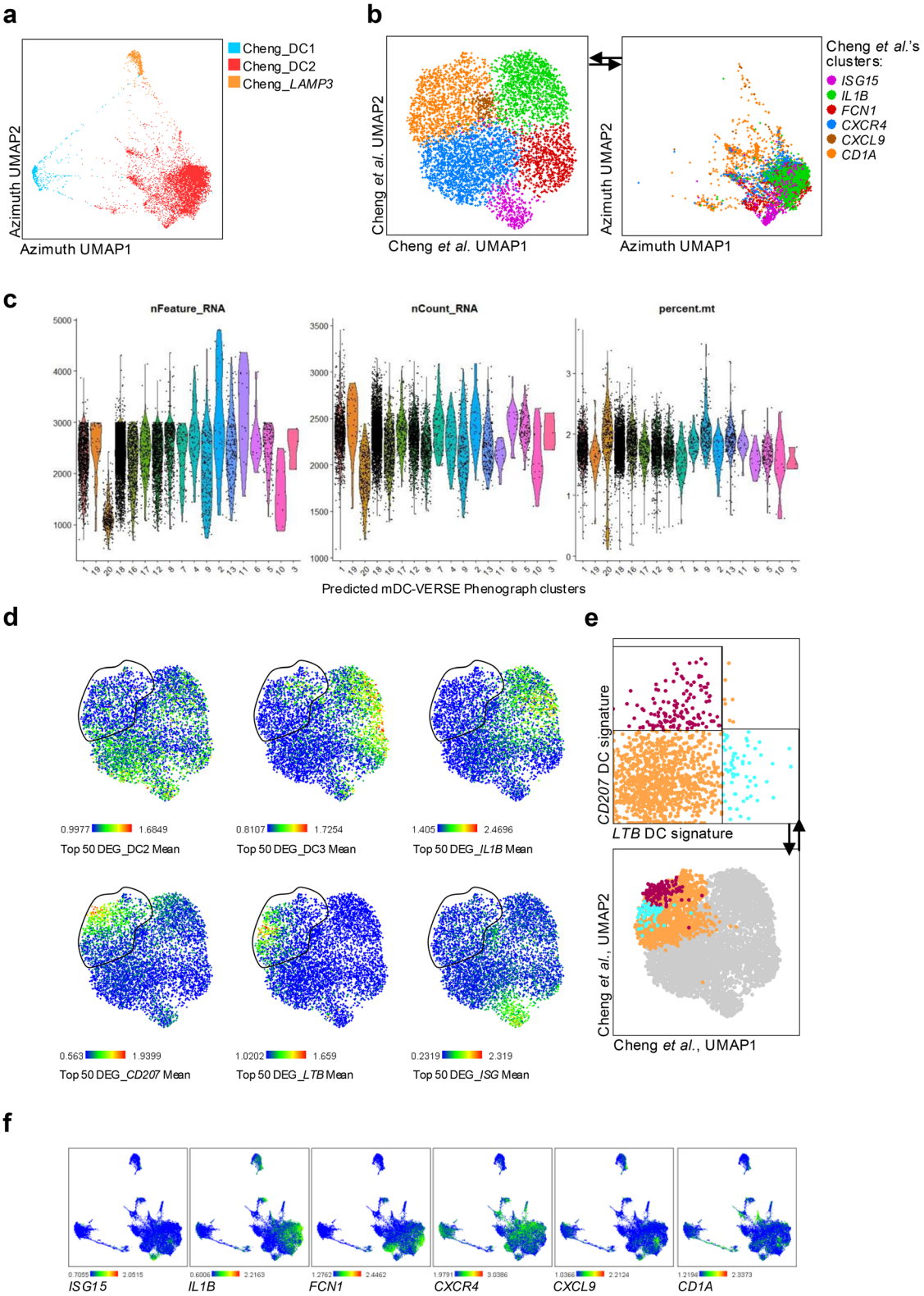

Extended Data Fig. 3 | Comparison of mDC-VERSE DC2 + DC3 populations to Cheng's cDC2 subsets. a-b, Projection of **a**, all mDC subsets and **b**, DC2 + DC3 populations defined by Cheng et al.'s metadata on the mDC-VERSE using multimodal reference mapping. **c**, Quality control metrics of predicted mDC-VERSE Phenograph clusters from Cheng et al. data projected by multimodal reference mapping. **d**, Mean expression of the top 50 genes of mega-clusters from the mDC-VERSE mapped onto the UMAP from Cheng et al. **e**, Mapping of cDC2_*CD1A* cells from Cheng et al., enriched in *CD207* or *LTB* DC signatures (from the mDC-VERSE) onto the UMAP from Cheng et al. **f**, Meaning plots of the mean gene signatures of DC2 + DC3 populations from Cheng et al. shown on the mDC-VERSE. Related to Fig. 2.

https://doi.org/10.1038/s41590-025-02337-x

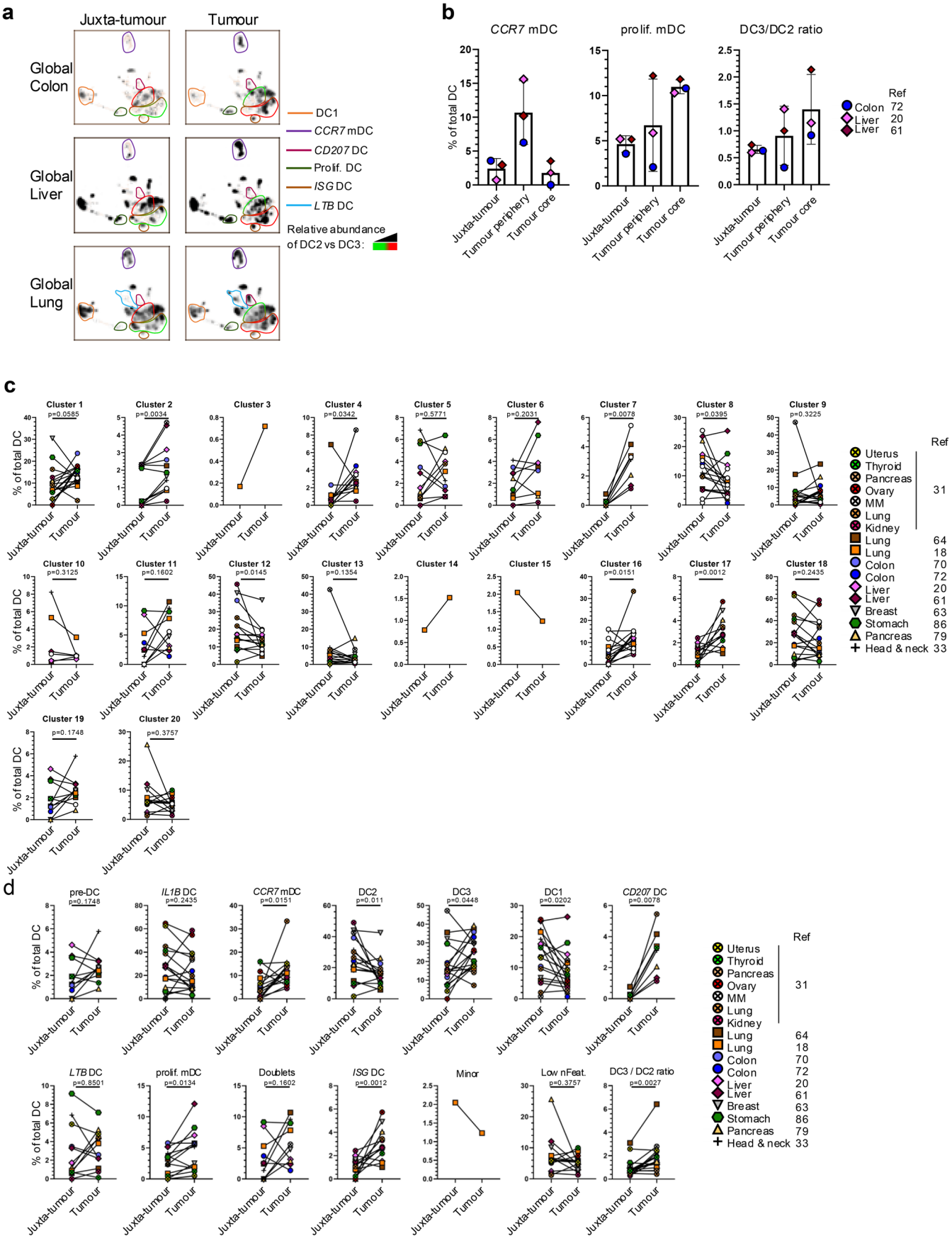

Extended Data Fig. 4 | See next page for caption.

https://doi.org/10.1038/s41590-025-02337-x

Extended Data Fig. 4 | Metadata analysis of mDC populations in cancer. **a**, Density plots of global colon, liver and lung datasets highlighting changes in DC1s, *CCR7* mDCs, *CD207* DCs, Prolif. DCs, *ISG* DCs and *LTB* DCs between juxta-tumoral and tumoral tissues. **b**, Percentage of *CCR7* mDCs and Prolif. DCs, and DC3/DC2 ratio in datasets which had analysed juxta-tumoral tissue, tumour periphery and tumour core. **c**,**d**, Percentage of mDC-VERSE **c**, phenograph clusters and **d**, mega clusters in all integrated and query datasets (Obtained through multimodal reference mapping and annotated with cross symbol) between matched juxta-tumoral and cancer tissues. See Supplementary Table 1 for the specified tumour types. P-values were calculated using a Wilcoxon non-parametric paired test. Related to Fig. 3.

https://doi.org/10.1038/s41590-025-02337-x

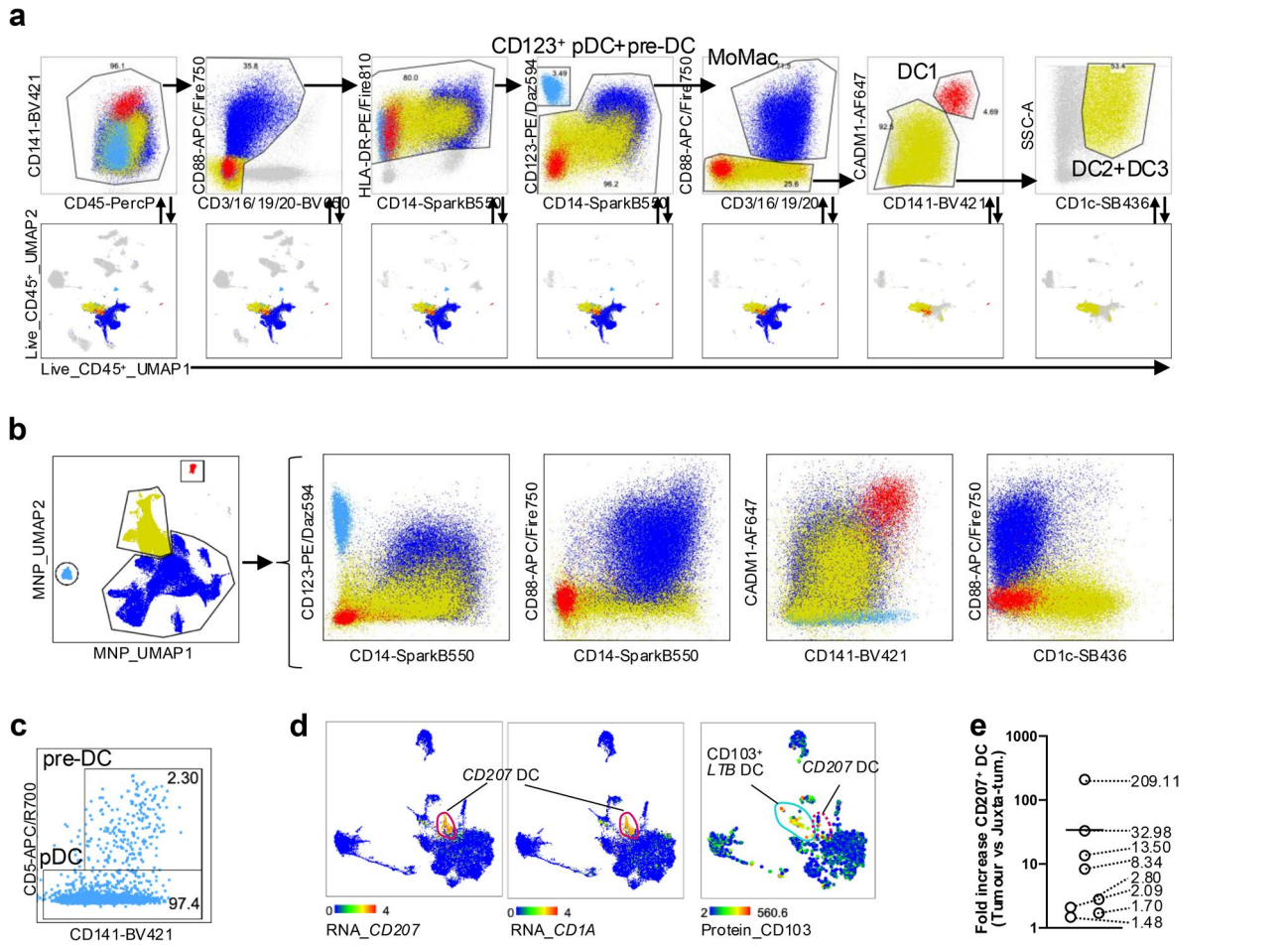

Extended Data Fig. 5 | Gating strategy to define DC populations and states and evaluation of their phenotype in NSCLC spectral flow cytometry data. **a**, Gating strategy from singlets, live, CD45$^+$ cells and projection of each gated population onto the Live_CD45$^+$_UMAP space. **b**, MNP extracted from the Live_CD45$^+$_UMAP were analysed by UMAP to generate the MNP_UMAP, whose annotation is confirmed by protein expression. **c**, Gating of pDCs and pre-DCs within CD123$^+$ DCs defined in Fig. 4a-b. **d**, RNA expression of *CD207* and *CD1A* and protein expression of CD103 overlaid on the mDC-VERSE. **e**, Fold increase of CD207$^+$ DCs in tumour versus matched juxta-tumoral tissue. Related to Fig. 4.

https://doi.org/10.1038/s41590-025-02337-x

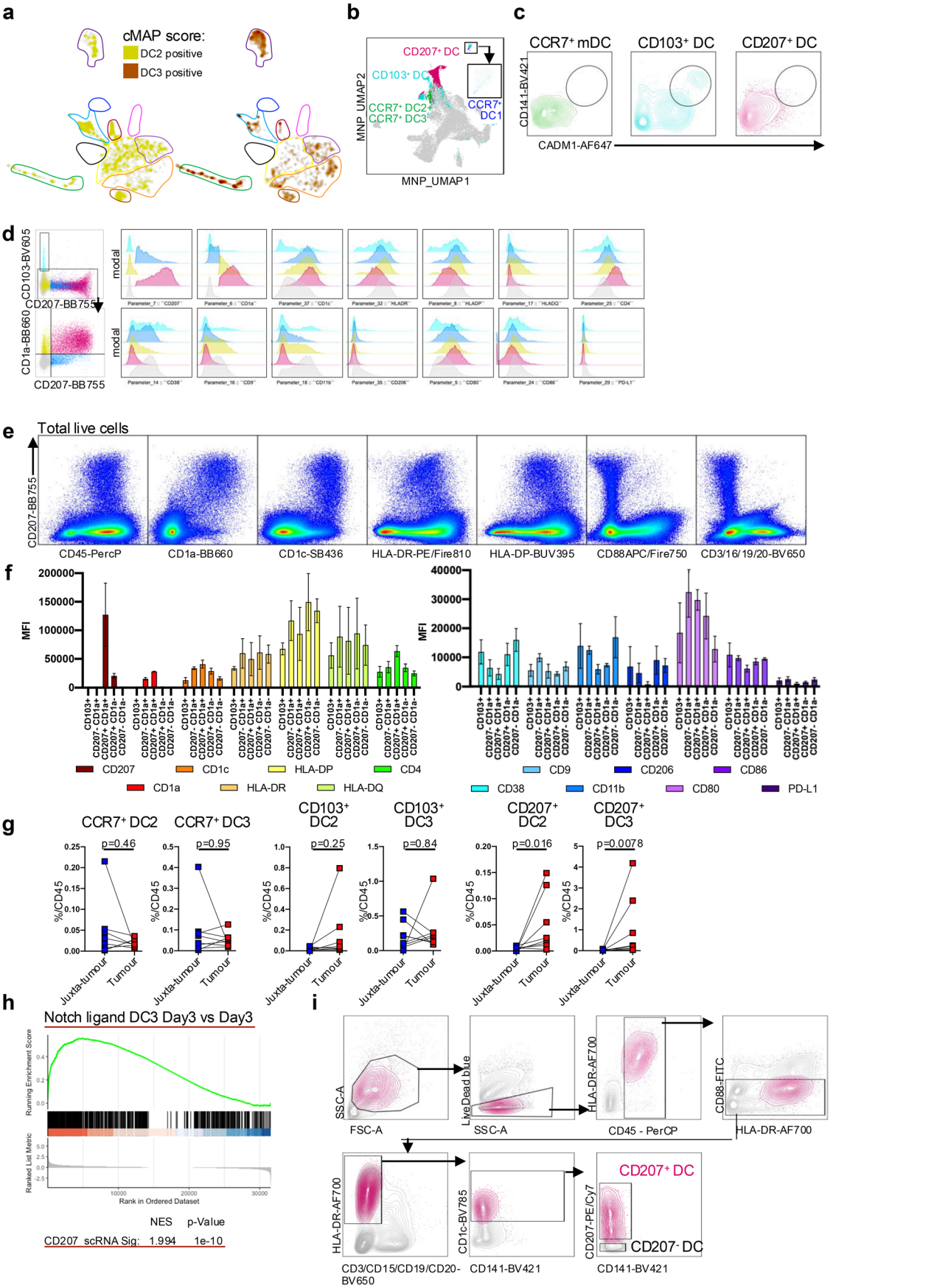

Extended Data Fig. 6 | See next page for caption.

https://doi.org/10.1038/s41590-025-02337-x

Extended Data Fig. 6 | Subset versus state consideration. a, Mapping of cMAP scores from Fig. 5b on the mDC-VERSE. **b**, Overlay of DC "states" identified in Fig. 5c onto the MNP_UMAP space. **c**, Expression of CADM1 and CD141 by CCR7$^+$ mDCs, CD103$^+$ DCs and CD207$^+$ DCs. **d**, Gating and phenotype of CD103$^+$ "*LTB*" and CD1a$^+$CD207$^+$ DCs. **e**, Expression of CD45, CD1a, CD1c, HLA-DR, HLA-DP, CD88 and CD3/CD16/CD19/CD20 versus CD207 by total live cells (including CD45$^-$ non-immune cells) from a NSCLC tumour. **f**, Mean fluorescence intensity (MFI) of markers expressed by populations of DCs defined in panel **d**. **g**, Percentage of DC "states" identified in (Fig. 5c and Fig. 5c) among total CD45$^+$ cells in matched juxta-tumoral tissue versus tumour. **h**, Gene set enrichment analysis (GSEA) of the *CD207* DC signature comparing bulk RNAseq of DC3s at day 3 cultured with GM-CSF + TGF-β with or without OP-9-D4 cells from Kvedaraite et al., 2022. (**i**) Gating strategy from singlets for the sorting of CD207$^+$ DCs in ovarian cancer. P-values were calculated using a Wilcoxon non-parametric paired test, two-tailed. Related to Fig. 5.

https://doi.org/10.1038/s41590-025-02337-x

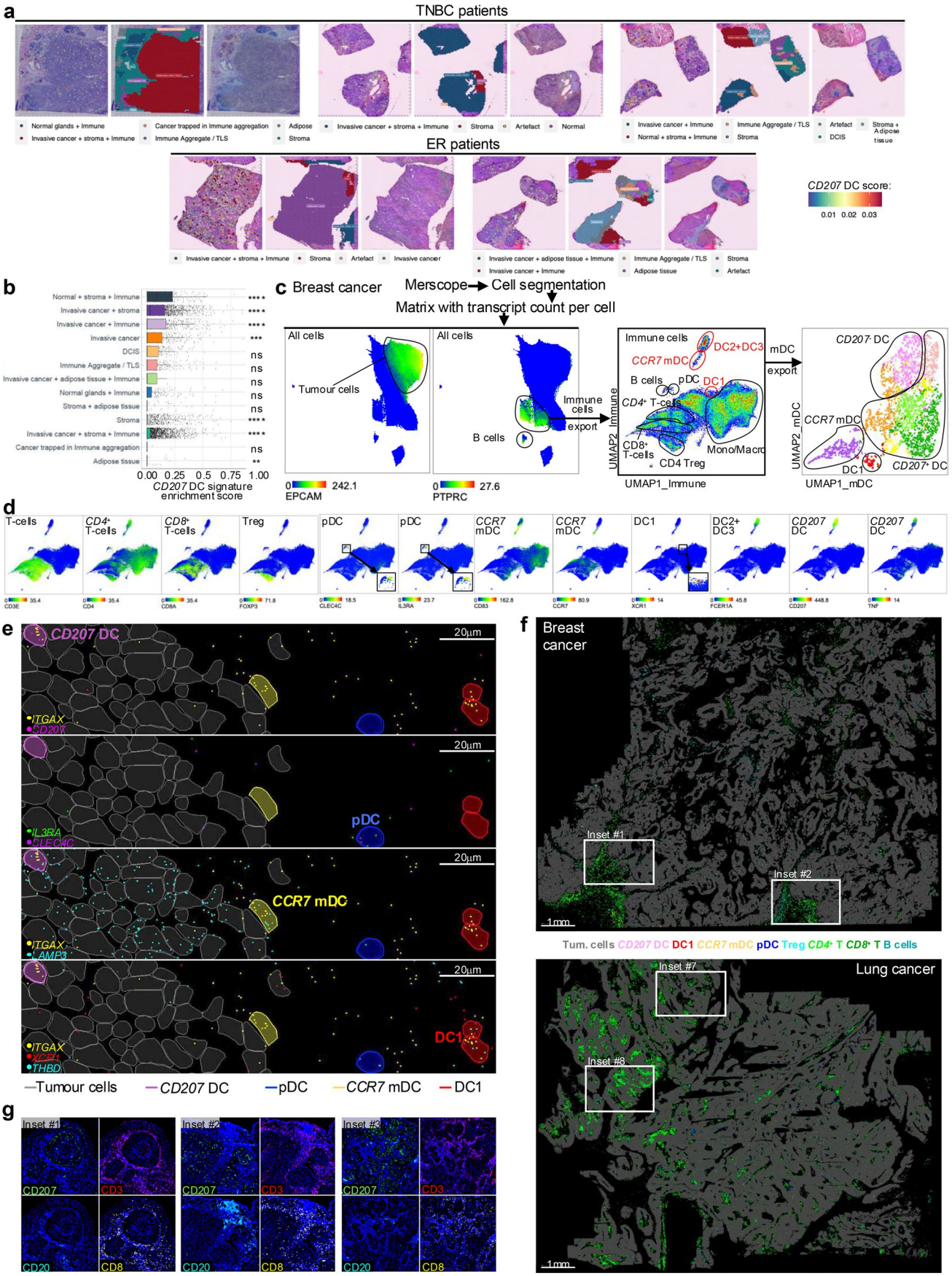

Extended Data Fig. 7 | See next page for caption.

https://doi.org/10.1038/s41590-025-02337-x

Extended Data Fig. 7 | Spatial mapping and characterisation of the pathophysiological involvement of DC populations in human breast and lung cancer patients. a, Visium spatial transcriptomic profiling of 3 TNBC and 2 ER breast cancer patients from Wu et al. For each patient, the left panel shows the *CD207* DC signature score, middle panel shows tissue niches, and the right panel shows haematoxylin and eosin (H&E) staining. **b**,) Enrichment score of *CD207* DC signature across different tissue niches identified in **a**. **c**, Meaning plots of *EPCAM* and *PTPRC* expression visualised on the UMAP generated with all cells from the Merscope data of the breast cancer patient. Immune cells were extracted, and different cell populations were annotated based on a curated list of genes. mDCs were then extracted to generate an mDC UMAP that identified mDC populations. **d**, Meaning plots of representative genes used to define the immune populations identified in the Immune cells' UMAP from panel **c**. **e,f**, Merfish analysis of breast cancer and lung cancer cross-sections. **e**, Visualisation of the expression of DC population-defining transcripts in the segmented Merfish spatial data. **f**, Spatial distribution of tumour cells (grey) and immune populations within the breast and lung tumour cross-sections analysed by Merfish. **g**, Single fluorescent images for CD207 (green), CD3 (red), CD8 (yellow) and CD20 (cyan) of the IHF data shown in Fig. 6g. * = $p < 0.05$, ** = $p < 0.005$, *** = $p < 0.005$ and **** = $p < 0.0005$. Related to Fig. 6.

https://doi.org/10.1038/s41590-025-02337-x

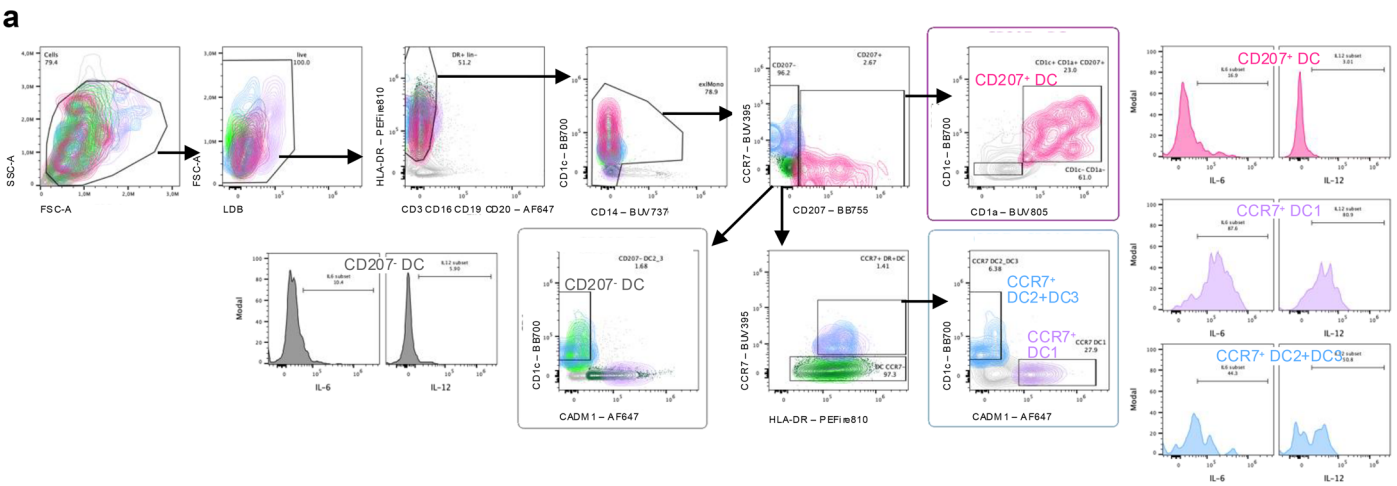

Extended Data Fig. 8 | Characterisation of functional mDC states in human cancer patients. a, Gating strategy for identifying mDC populations in the ICS experiment (see Fig. 7a-d). **b**, Percentage of positive cells for co-stimulatory factors in, (Left) CD1c$^+$ DC2/3 CD207$^{+/-}$, (Middle) CADM1$^+$ DC1 CCR7$^{+/-}$, (Right) CD1c$^+$DC2/3 CCR7$^{+/-}$. P-values were calculated using a Wilcoxon non-parametric paired test, two-tailed. Related to Fig. 7.

https://doi.org/10.1038/s41590-025-02337-x

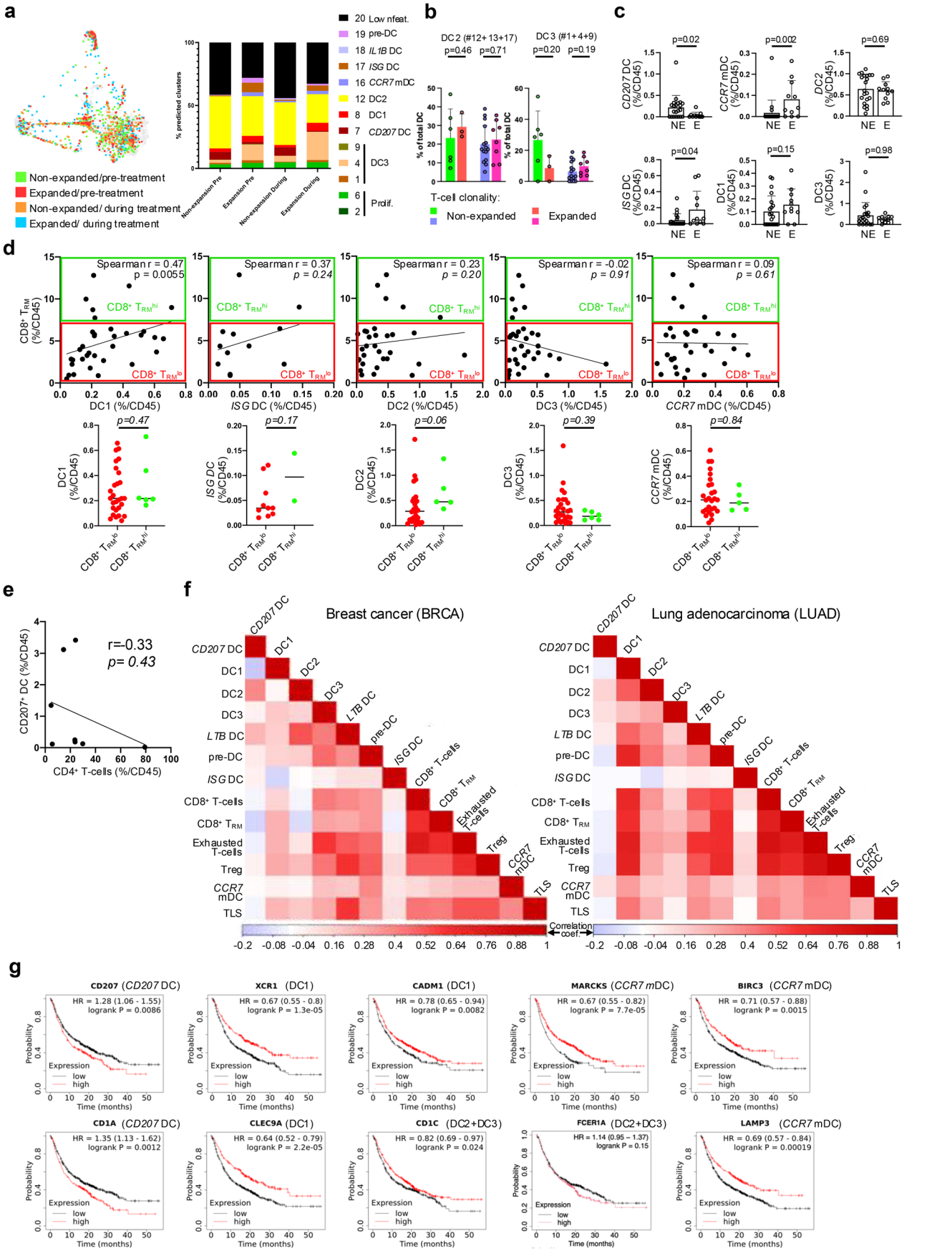

Extended Data Fig. 9 | See next page for caption.

https://doi.org/10.1038/s41590-025-02337-x

Extended Data Fig. 9 | Characterisation of the pathophysiological involvement of mDC populations in human cancer patients. a, Percentage of predicted phenograph clusters from query dataset (Bassez et al.) projected using multimodal reference mapping onto the mDC-VERSE. **b**, Percentage of predicted DC2 and DC3 mega-clusters by multimodal reference mapping of query data from breast cancer patients categorised by T-cell clonality and treatment status (anti-PD-1 therapeutic monoclonal antibody = Immune Checkpoint Blockade = ICB). **c**, Percentage of *CD207* DCs, *CCR7* mDC, *ISG* DC and DC1 between patients with non-expanded and expanded T-cell clonality in the Bassez et al. data. **d**, Upper panel shows the correlation between the frequencies among $CD45^+$ cells of DC populations (DC1s, *ISG* DCs, DC2s, DC3s and *CCR7* mDCs) and CD8 T_{RMs} in lung tumours within the Leader et al. scRNAseq data. Lower panel shows the frequencies among *PTPRC*(CD45)-expressing immune cells of the same DC populations split by *CD8* T_{RMs}^{hi} and *CD8* T_{RMs}^{lo}. **e**, Correlation between the frequencies of $CD207^+$ DCs and $CD4^+$ T-cells from flow cytometry analysis of 8 NSCLC patients. **f**, Correlation map of DC population signatures (defined in the mDC-VERSE) and of other signatures obtained from Ramos et al. in the BRCA (Breast) and the LUAD (Lung) adenocarcinoma TCGA datasets. **g**, Kaplan-Meier plots of the overall survival (OS) of patients with different cancers whose tumour was sampled and analysed by bulk RNAseq prior to immune checkpoint blockade (ICB) treatment. Patients were separated based on high or low expression of genes specifically expressed by total DC2s + DC3s, by *CD207* DCs, by DC1s or by *CCR7* mDCs. Correlations were evaluated using the Pearson correlation (r) with two-tailed p values. P-values were calculated using a Wilcoxon non-parametric paired test, two-tailed. Related to Fig. 7.

nature portfolio

Corresponding author(s): Florent Ginhoux, Charles-Antoine Dutertre

Last updated by author(s): Oct 8, 2025

Reporting Summary

Nature Portfolio wishes to improve the reproducibility of the work that we publish. This form provides structure for consistency and transparency in reporting. For further information on Nature Portfolio policies, see our Editorial Policies and the Editorial Policy Checklist.

Statistics

For all statistical analyses, confirm that the following items are present in the figure legend, table legend, main text, or Methods section.

n/a	Confirmed
☐	☒ The exact sample size (*n*) for each experimental group/condition, given as a discrete number and unit of measurement
☒	☐ A statement on whether measurements were taken from distinct samples or whether the same sample was measured repeatedly
☐	☒ The statistical test(s) used AND whether they are one- or two-sided *Only common tests should be described solely by name; describe more complex techniques in the Methods section.*
☒	☐ A description of all covariates tested
☒	☐ A description of any assumptions or corrections, such as tests of normality and adjustment for multiple comparisons
☐	☒ A full description of the statistical parameters including central tendency (e.g. means) or other basic estimates (e.g. regression coefficient) AND variation (e.g. standard deviation) or associated estimates of uncertainty (e.g. confidence intervals)
☐	☒ For null hypothesis testing, the test statistic (e.g. *F*, *t*, *r*) with confidence intervals, effect sizes, degrees of freedom and *P* value noted *Give P values as exact values whenever suitable.*
☒	☐ For Bayesian analysis, information on the choice of priors and Markov chain Monte Carlo settings
☒	☐ For hierarchical and complex designs, identification of the appropriate level for tests and full reporting of outcomes
☐	☒ Estimates of effect sizes (e.g. Cohen's *d*, Pearson's *r*), indicating how they were calculated

Our web collection on statistics for biologists contains articles on many of the points above.

Software and code

Policy information about availability of computer code

Data collection	The DC-VERSE and the mDC-VERSE can be explored and downloaded at https://github.com/gustaveroussy/FG-Lab
Data analysis	See the method section for details, and code deposit can be explored at https://github.com/gustaveroussy/FG-Lab

For manuscripts utilizing custom algorithms or software that are central to the research but not yet described in published literature, software must be made available to editors and reviewers. We strongly encourage code deposition in a community repository (e.g. GitHub). See the Nature Portfolio guidelines for submitting code & software for further information.

Data

Policy information about availability of data

All manuscripts must include a data availability statement. This statement should provide the following information, where applicable:

- Accession codes, unique identifiers, or web links for publicly available datasets
- A description of any restrictions on data availability
- For clinical datasets or third party data, please ensure that the statement adheres to our policy

The DC-VERSE and the mDC-VERSE can be explored and downloaded at https://github.com/gustaveroussy/FG-Lab .

Human research participants

Policy information about studies involving human research participants and Sex and Gender in Research.

Reporting on sex and gender	No informations were available on samples analyzed by spectral flow cytometry.
Population characteristics	No informations were available on samples analyzed by spectral flow cytometry.
Recruitment	Tumour and normal adjacent tissue from the lung, as well as FFPE blocks, were obtained from Non-Small Cell Lung Cancer patients following written informed consent (Marie Lannelongue Hospital, Paris) and ethical approval (N°ID-RCB: 2016-A00732-49). All subjects provided IRB-approved consent. Human tissues were cut into 0.5 cm squares and incubated with 0.8 mg/mL collagenase (Type IV, Worthington-Biochemical) in RPMI (PAA) with 10% FCS (AutogenBioclear) for 2 and 8 h, respectively, or when stated mechanically dispersed.
Ethics oversight	ethical approval N°ID-RCB: 2016-A00732-49, Gustave Roussy, France

Note that full information on the approval of the study protocol must also be provided in the manuscript.

Field-specific reporting

Please select the one below that is the best fit for your research. If you are not sure, read the appropriate sections before making your selection.

☒ Life sciences ☐ Behavioural & social sciences ☐ Ecological, evolutionary & environmental sciences

For a reference copy of the document with all sections, see nature.com/documents/nr-reporting-summary-flat.pdf

Life sciences study design

All studies must disclose on these points even when the disclosure is negative.

Sample size	8 cancer patients.
Data exclusions	no exclusion
Replication	N/A
Randomization	N/A
Blinding	investigators were blinded

Reporting for specific materials, systems and methods

We require information from authors about some types of materials, experimental systems and methods used in many studies. Here, indicate whether each material, system or method listed is relevant to your study. If you are not sure if a list item applies to your research, read the appropriate section before selecting a response.

Materials & experimental systems

n/a	Involved in the study
☐	☒ Antibodies
☒	☐ Eukaryotic cell lines
☒	☐ Palaeontology and archaeology
☒	☐ Animals and other organisms
☒	☐ Clinical data
☒	☐ Dual use research of concern

Methods

n/a	Involved in the study
☒	☐ ChIP-seq
☐	☒ Flow cytometry
☒	☐ MRI-based neuroimaging

Antibodies

Antibodies used	Anti-goat (Polyclonal) AF488, Jackson Immuno-Research Laboratory, Cat# 705-545-147, RRID:AB_2336933 CCR2 (Clone LS132.1D9) BUV563, BD Biosciences, Cat# 749076, RRID:AB_2873470 CD11b (Clone M1/70) BV570, Biolegend, Cat# 101233, RRID:AB_10896949 CD117 (Clone 104D2) APC, Biolegend, Cat# 313206, RRID:AB_314985

CD123 (Clone 6H6) PE/Daz594, Biolegend, Cat# 306034, RRID:AB_2566450
CD103 (Clone Ber-ACT8) BV605, Biolegend, Cat# 350217, RRID:AB_2564282
CD14 (Clone 63D3) SparkB550, Biolegend, Cat# 367148, RRID:AB_2832724
CD141 (Clone M81) BV421, Biolegend, Cat# 344114, RRID:AB_2562956
CD169 (Clone 7-239) BUV661, BD Biosciences, Cat# 750363, RRID:AB_2874538
CD19 (Clone HIB19) BV650, Biolegend, Cat# 302238, RRID:AB_2562097
CD1a (Clone SK9) BB660, BD Biosciences, Custom
CD1c (Clone L161) SB436, Invitrogen, Cat# 62-0015-42, RRID:AB_2762426
CD20 (Clone 2H7) BV650, Biolegend, Cat# 302336, RRID:AB_2563806
CD25 (Clone CD25-3G10) PE/AF700, Thermo Fisher Scientific, Cat# MHCD2524, RRID:AB_2539740
CD206 (Clone 19.2) PercP/eFluor 710, Thermo Fisher Scientific, Cat# 46-2069-42, RRID:AB_10853034
CD207 (Clone 2G3) BB755, BD Biosciences, Custom
CD209 (Clone 9E9A8) PE/Cy7, Biolegend, Cat# 330114, RRID:AB_10719953
CD3 (Clone SP34-2) BV650, BD Biosciences, Cat# 563916, RRID:AB_2738486
CD301 (Clone H037G3) PE, Biolegend, Cat# 354704, RRID:AB_11219002
CD38 (Clone HB7) BUV805, BD Biosciences, Cat# 742074, RRID:AB_2871359
CD4 (Clone SK3) Cfl.YG584, Cytek Biosciences, Cat# R7-20041, RRID:AB_2885083
CD45 (Clone 30-F11) PercP, Biolegend, Cat# 103130, RRID:AB_893339
CD5 (Clone UCHT2) APC/R700, BD Biosciences, Cat# 565121, RRID:AB_2744433
CD8 (Clone SK1) APC/Fire 810, Biolegend, Cat# 344764, RRID:AB_2860890
CD127 (Clone HIL-7R-M21) BB510, BD Biosciences, Custom
CD86 (Clone 2331) BV786, BD Biosciences, Cat# 740990, RRID:AB_2870657
CD88 (Clone S5/1) APC/Fire750, Biolegend, Cat# 344316, RRID:AB_2750445
CD89 (Clone A59) BUV496, BD Biosciences, Cat# 750617, RRID:AB_2874749
CD9 (Clone M-L13) BV480, BD Biosciences, Cat# 746356, RRID:AB_2743675
FcεRIα (Clone AER-37 (CRA-1)) BV711, Biolegend, Cat# 334638, RRID:AB_2687186
HLA-ABC (Clone W6/32) Sp. NIR 685, Biolegend, Cat# 311453, RRID:AB_2876612
HLA-DP (Clone B7/21) BUV395, BD Biosciences, Cat# 750866, RRID:AB_2874962
HLA-DQ (Clone Tu169) BV510, BD Biosciences, Cat# 742609, RRID:AB_2740907
HLA-DR (Clone L243) PE/Fire 810, Biolegend, Custom
PD-L1 (Clone MIH1) PE/Cy5, Invitrogen, Cat# 15-5983-42, RRID:AB_2802211
PD1 (Clone EH12.1) BV750, BD Biosciences, Cat# 747446, RRID:AB_2872125
SLAN (Clone DD-1) VioBlue, Miltenyi Biotec, Cat# 130-119-868, RRID:AB_2733608
CADM1 (Clone 3E1), MBL International, Cat# CM004-3, RRID:AB_592783
IRF4 (Clone 3E4) PE, Thermo Fisher Scientific, Cat# 12-9858-82, RRID:AB_10852721
IRF8 (Clone V3GYWCH) PercP/eFluor 710, Thermo Fisher Scientific, Cat# 46-9852-82, RRID:AB_2573904
CD11c (Clone 3.9) BV605, BioLegend , Cat# 301636, RRID:AB_2563796
CD16 (Clone 3G8) APC/Cy7, BioLegend , Cat# 302017, RRID:AB_314217
HLA-DR (Clone L243) BV785, BioLegend , Cat# 307641, RRID:AB_2561360
CD14 (Clone RMO52) ECD, Beckamn Coulter, Cat# B92391
CD123 (Clone 7G3) BUV395, BD Biosciences , Cat# 564195, RRID:AB_2714171
CD45 (Clone HI30) V500, BD Biosciences , Cat# 560777, RRID:AB_1937324
ViaDye™ Red Fixable Viability Dye Kit, Cytek Biosciences, Cat# SKU R7-60008
LIVE/DEAD™ Fixable Blue Dead Cell, Invitrogen, Cat# L23105
CCR7 (Clone 2-L1-A) BUV737, BD Biosciences, Cat# 749676, RRID:AB_2873937

Validation

Dilutions were used as recommended by the supplier.

Flow Cytometry

Plots

Confirm that:

☐ The axis labels state the marker and fluorochrome used (e.g. CD4-FITC).

☐ The axis scales are clearly visible. Include numbers along axes only for bottom left plot of group (a 'group' is an analysis of identical markers).

☒ All plots are contour plots with outliers or pseudocolor plots.

☒ A numerical value for number of cells or percentage (with statistics) is provided.

Methodology

Sample preparation

Intranuclear staining of IRF4 and IRF8 was performed as mentioned in Guilliams et al.(ref 9). Briefly, cells were thawed, washed and incubated with Live/Dead blue dye (30 min, 4°C; Invitrogen/Life Technologies) in PBS. Then, 5% heat-inactivated fetal calf serum (FCS) was added (15 min, 4°C; Sigma Aldrich). Cells were labelled with antibodies (PBS-2% FCS and 2 mM EDTA, 30 min, 4°C), then washed and stained with secondary reagents. Cells were stained intracellularly for IRF8 and/or IRF4 using the eBioscience FOXP3 / Transcription Factor Staining Buffer Set (eBioscience/Affymetrix) following the manufacturer's instructions. The samples were acquired using a FACS FORTESSA (BD Biosciences). FCS files were exported and analysed using FlowJo v10.8.1.
For the NSCLC normal adjacent and tumour samples, cells were thawed and transferred into RPMI (Thermo Fischer) with 20% decomplemented FCS (Thermo Fischer). Samples were treated with 1mg/ml DNase I (Sigma-Aldrich) at 37°C. Cells were incubated with Live/Dead blue dye (Invitrogen) for 30 min at 4°C in phosphate buffered saline (PBS) and then incubated in 5%

	heat-inactivated fetal calf serum (FCS, Sigma Aldrich) for 15 min at 4°C. Cells were stained with appropriate antibodies (listed in the methods resources table and Table S5 in PBS with 2% FCS, 2mM EDTA (Sigma Aldrich) and Brilliant Stain buffer (BD), incubated for 30 min at 4°C, and then washed. Cells were analysed using a Cytek Aurora 5-laser spectral analyser. FCS files were exported and analysed using FlowJo v10.8.1.
Instrument	Cytek Aurora 5-laser spectral analyser
Software	Flow Jo 10
Cell population abundance	Total tumour cells were thawed and analyzed, without prior enrichment.
Gating strategy	Gating strategies are described in Figures.

☒ Tick this box to confirm that a figure exemplifying the gating strategy is provided in the Supplementary Information.